AD-A081 710 SPERRY RESEARCH CENTER SUDBURY MASS F/G 20/1
ACTIVE SONAR MODELING.(U)
AUG 78 H MIERAS, C L BENNETT N61339-77-C-0105
UNCLASSIFIED SCRC-CR-78-44 NL

1 OF 2
AD A081710

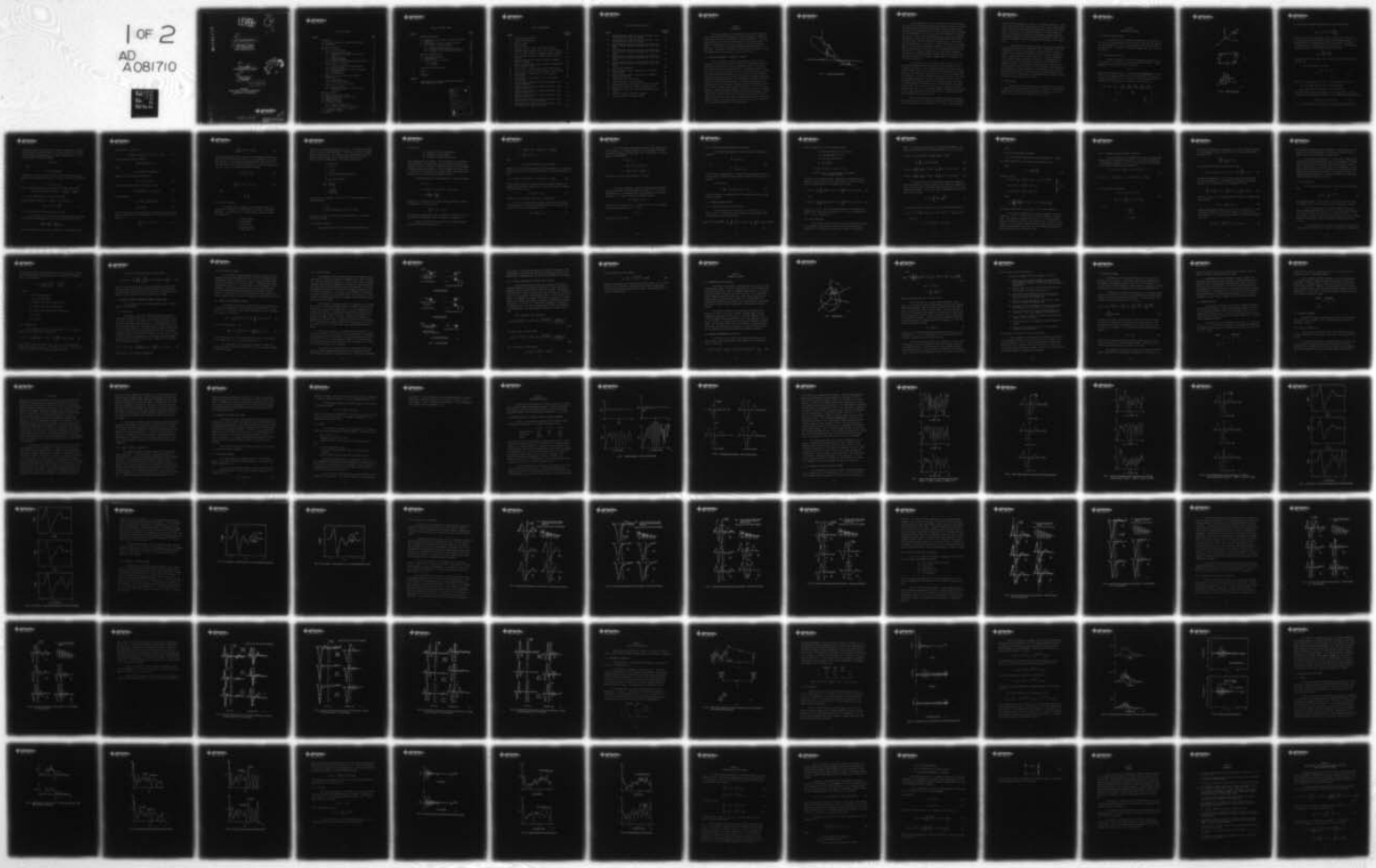

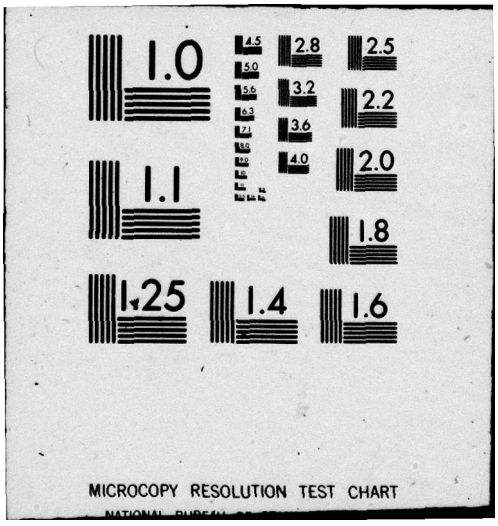
1.0
1.1
1.25
1.4
1.6
1.8
2.0
2.2
2.5
2.8
3.2
3.6
4.0
4.5
5.0
5.6
6.3
7.1
8.0
9.0
MICROCOPY RESOLUTION TEST CHART

LEVEL IV

3

ACTIVE SONAR MODELING

H. Mieras and C. L. Bennett
Sperry Research Center
Sudbury, Massachusetts 01776

FINAL REPORT
Contract No. N61339-77-C-0105

SCRC-CR-78-44
August 1978
101

Prepared for
NAVAL COASTAL SYSTEMS LABORATORY
PANAMA CITY, FLORIDA 32407

SPERRY
RESEARCH CENTER

SPERRY
RESEARCH CENTER

TABLE OF CONTENTS

SPERRY
RESEARCH CENTER

TABLE OF CONTENTS (CONTD)

SPERRY RESEARCH CENTER

LIST OF ILLUSTRATIONS

LIST OF ILLUSTRATIONS (contd)

SECTION 1
INTRODUCTION

The general problem to be considered here is acoustic scattering in the resonance region from arbitrarily shaped 3-dimensional targets in a fluid medium, possibly in the presence of a bottom ~~(see Fig. 1)~~. The techniques presented in this report can be applied to the general problem. For purposes of tractability at this initial stage, scattering from elastic targets is considered for rotationally symmetric homogeneous targets in free water. The problem of scattering in the presence of a bottom is solved for sound-hard and -soft targets on a hard or soft bottom.

1.1 HISTORICAL BACKGROUND - COMPARISON OF METHODS

The calculation of acoustic scattering from an elastic solid submerged in a fluid needs to take into account the compressional and shear waves inside the solid as well as the compressional wave in the medium. The problem was first solved, analytically, in the frequency domain, for the special case of the sphere by Faran [1]. His method consists of writing the general eigenfunction expansions of the three waves in the frequency domain and solving for the coefficients by applying the boundary conditions. Hickling [2] published results of calculations based on Faran's solution for spheres of several different materials. An eigenfunction solution is restricted for use with very special geometries, such as the sphere and infinite cylinder at normal incidence considered by Faran. The result of this method is a complete frequency response. Prior to Faran's work, the problem was solved in a similar fashion by Anderson [12] for fluid targets. Fluid targets lack a shear wave and can be considered a special case of elastic target. As part of the current effort, calculations were made based on the above solutions for an elastic sphere in order to check out the solution by the more general formulation to be described below.

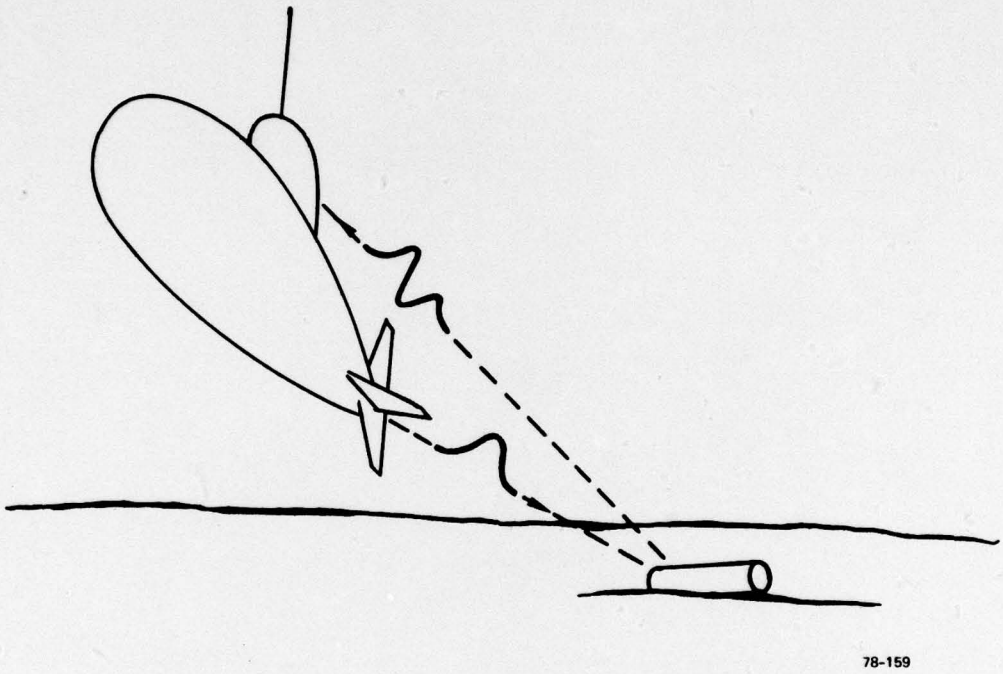

FIG. 1 General scattering problem.

Another approach is to write the solutions to the wave equations as integrals over the bounding surface using Green's function. This method has been used extensively for electromagnetic scattering problems and to some extent for acoustic problems. For scattering from a perfect conductor in the electromagnetic case, or from a perfectly sound-hard or sound-soft target in the acoustic case, this method results in one integral equation. The equation is solved first for the surface field values, and is then used with surface values to compute the scattered field. The solution of the integral equation on the surface is usually performed in the frequency domain; either by using eigenfunction expansions [3] (which has the same geometry restrictions as noted above), or by integrating numerically over the surface [4]. Numerical integration frees the problem of geometry restrictions. The frequency domain solution requires the inversion of an N x N matrix, where N is the number of sample points on the surface, for each value of frequency.

The approach taken at the Sperry Research Center is to solve the integral equation numerically directly in the time domain [5], by stepping the solution in time; a technique named the space-time integral equation (STIE) approach. This procedure eliminates the need for a matrix inversion. The time domain response can then be convolved inversely with the excitation to obtain the frequency response of the target. This resultant broadband response is valid from zero frequency to an upper limit determined by the frequency content of the excitation pulse. The latter is limited primarily by computation time. Practical values of the upper frequency limit are $ka = 6$ to 12. As this range of frequencies includes the resonance region, it is particularly capable of relating target response to size, shape, and material. The relative merits of frequency and time domain approaches are discussed in [6].

For the elastic problem, three integral equations are required: two scalar equations for the compressional waves in the target and medium, and a vector equation for the shear wave in the target. These equations

must be solved simultaneously, subject to the boundary conditions. Depending on the variables used, these can lead to rather complex integral equations. Hence, the first problem is the appropriate choice of field variables. In this report, the curl and divergence of the displacement are chosen, since these yield relatively straightforward integral equations and boundary relations. Fluid, sound-hard, and sound-soft targets can be treated as degenerate cases of the general elastic target in this formulation.

Other approaches of interest are the physical optics approximation and the geometrical theory of diffraction (GTD). The physical optics approximation is based on the observation that in the limit of very high frequency (for a sound-hard or sound-soft target), the ramp response of a target is proportional to the area function (i.e., the area illuminated by the incident ramp as a function of time) [7]. This approximation is used here for predicting the asymptotic behavior of the response as the frequency increases. The GTD proceeds by calculating the response and relative phase of each discontinuity (scattering center) of the target and then combining the separate responses at the appropriate relative phases. This theory applies only at high frequencies since the interaction of the surface with itself (creep waves) is neglected; however it predicts readily the effect of aspect change on the response.

1.2 VERIFICATION

The general STIE solution has been checked for the elastic sphere by comparison with the eigenfunction solution. In addition, the calculated responses were compared with measurements taken at NCSL on a variety of targets. The results will be discussed in Sections 4 and 5.

SECTION 2
THEORETICAL FOUNDATION

2.1 PHYSICS OF ELASTIC SOLIDS

The derivation of the acoustic wave equations in fluids and elastic solids will be presented in outline in order to make clear the meaning of certain variables to be used in the development of the STIE solution in the next section. The reader is referred to a modern text, such as [8] for more detail.

2.1.1 Generalized Hooke's Law

Consider an element of matter, infinitesimal but continuous (i.e., not a particle), at position $\bar{r}$ in a cartesian coordinate system. Its <u>displacement</u> from equilibrium position is given by

$$\bar{u} = d\bar{r} \ ,$$

and the total deformation by $d\bar{u}$. To obtain the <u>true deformation</u>, or strain, the change in displacement due to a pure rotation about $\bar{r}$ is subtracted from $d\bar{u}$, namely $\frac{1}{2}(\nabla \times \bar{u}) \times \bar{u}$ [8]. Forming the total vector differential and subtracting the rotation term, one obtains the strain tensor D:

$$D = \begin{vmatrix} D_{xx} & D_{xy} & D_{xz} \\ \cdot & & \cdot \\ \cdot & \cdot & D_{zz} \end{vmatrix} = \begin{vmatrix} \frac{\partial u_x}{\partial x} & \frac{1}{2}\left(\frac{\partial u_y}{\partial x} + \frac{\partial u_x}{\partial y}\right) & \frac{1}{2}\left(\frac{\partial u_z}{\partial x} + \frac{\partial u_x}{\partial z}\right) \\ \cdot & \frac{\partial u_y}{\partial y} & \cdot \\ \cdot & \cdot & \frac{\partial u_z}{\partial z} \end{vmatrix} \qquad (1)$$

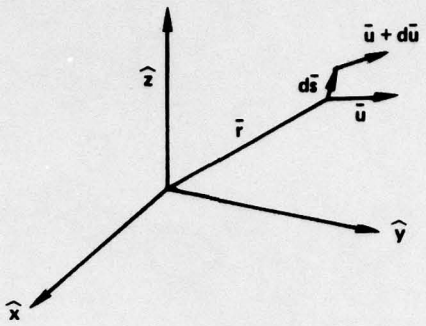

(a)

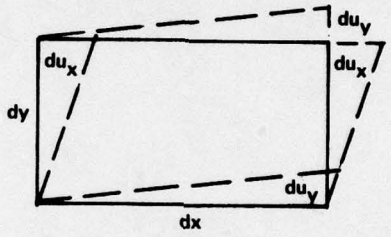

(b)

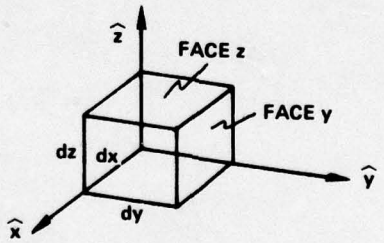

(c)

78-160

FIG. 2 Stress-strain relations.

so that the true deformation can be written as the matrix product

$$d\bar{u}_{true} = [\hat{x}, \hat{y}, \hat{z}] \; [D] \begin{bmatrix} dx \\ dy \\ dz \end{bmatrix} ,$$

where $\hat{x}$, $\hat{y}$, $\hat{z}$ are the cartesian unit vectors, and $\vec{ds} = \hat{x}\,dx + \hat{y}\,dy + \hat{z}\,dz$ is the differential change of position within the infinitesimal element. The interpretation of the diagonal terms of D is that $\partial u_x/\partial x$ is the linear (or "dilational") stress component in the x direction, i.e., the fractional increase in length. The off-diagonal terms, for instance

$$D_{xy} = \frac{1}{2}\left(\frac{\partial u_y}{\partial x} + \frac{\partial u_x}{\partial y}\right)$$

represents one half of the sum of the two shearing angles about the z-axis (see Fig. 2b).

The stress tensor S is written

$$S = \begin{Vmatrix} S_{xx} & S_{xy} & S_{xz} \\ . & . & . \\ . & . & S_{zz} \end{Vmatrix} \qquad (2)$$

Here, S_{zz} is the normal stress on face z in the $\hat{z}$ direction (Fig. 2c);

S_{zx} is the shear stress on face z in the $\hat{x}$ direction;

S_{zy} is the shear stress on face z in the $\hat{y}$ direction.

The form of Hooke's Law is that Modulus "times" strain = stress. For the dilational strain the physical relation is (in a homogeneous, isotropic solid)

$$Y D_{xx} = S_{xx} - \sigma(S_{yy} + S_{zz}) , \qquad (3)$$

i.e., the linear strain in the $\hat{x}$ direction is proportional to the sum of

the normal stress on the x face plus a contraction proportional to normal stresses applied to the other faces. Y is Young's modulus, σ is Poisson's ratio. Similar expressions hold for the other diagonal terms of D. For the shear strains, we have for example

$$2\mu\, D_{xy} = S_{xy} \tag{4}$$

where

μ is the shear modulus,

(the factor of 2 here, is due to the factor 1/2 in the definition of D_{xy}). Equation (3) can be solved for S_{xx}, etc., so that (3) and (4) can be written as

$$S = \lambda(\nabla \cdot \bar{u})\ I + 2\mu\, D \tag{5}$$

This is the generalized Hooke's Law relating stress and strain; where

λ is known as the Lamé coefficient, $\lambda = \frac{Y}{3(1-2\sigma)} - \frac{Y}{3(1+\sigma)}$,

$(\nabla \cdot \bar{u})$ is the dilation (or total linear strain).

The upper diagonal component, for example, of this equation is

$$S_{xx} = \lambda(\nabla \cdot \bar{u}) + 2\mu \frac{\partial u_x}{\partial x} \tag{5'}$$

2.1.2 Wave Equations in Elastic Solids and in Fluids

The $\hat{x}$ component of the total force on element (dx dy dz) is the sum of differences between opposing faces of all the $\hat{x}$ components of stress:

$$\left(\frac{\partial S_{xx}}{\partial x} + \frac{\partial S_{yx}}{\partial y} + \frac{\partial S_{zx}}{\partial z}\right) dx\, dy\, dz\ ,$$

with similar equations for the y and z components. Using equations (5) we

can thus write in vector form

$$\text{Force/unit volume} = (\lambda + \mu)\ \nabla(\nabla \cdot \bar{u}) + \mu \nabla^2 \bar{u} \tag{6}$$

It can be shown [8] that for small $\dot{\bar{u}}$,

$$\text{Force/unit volume} = \rho\, \ddot{\bar{u}} \tag{7}$$

where

ρ is the density of the material.

Equating (6) and (7) and using the identity

$$\nabla^2 \bar{u} = \nabla(\nabla \cdot \bar{u}) - \nabla \times \nabla \times \bar{u} \tag{8}$$

we obtain the desired equation of motion in a solid:

$$\ddot{\bar{u}} = \left(\frac{\lambda + 2\mu}{\rho}\right) \nabla(\nabla \cdot \bar{u}) - \frac{\mu}{\rho} \nabla \times \nabla \times \bar{u} \ . \tag{9}$$

We now substitute

$$c_1^2 = \frac{\lambda + 2\mu}{\rho} \text{ (compressional)} \tag{10}$$

$$c_2^2 = \frac{\mu}{\rho} \text{ (shear)} \tag{11}$$

These are identified as the compressional and shear wave velocities, upon taking the divergence and curl of equation (9). The results are the wave equations

$$\frac{\partial^2}{c_1^2\, \partial t^2} (\nabla \cdot \bar{u}) = \nabla^2 (\nabla \cdot \bar{u}) \tag{12}$$

$$\frac{\partial^2}{c_2^2 \partial t^2} (\nabla \times \bar{u}) = \nabla^2 (\nabla \times \bar{u}) \tag{13}$$

These are the equations to be solved by the STIE technique of Section 2.2. They state that the divergence and curl of the displacement each satisfy wave equations. In the fluid medium surrounding the solid, there is no shear stress, so that we have only equation (12) or the first term of equation (9). Using 3 as a subscript denoting the medium:

$$\ddot{\bar{u}}_3 = \frac{\lambda_3}{\rho_3} \nabla (\nabla \cdot \bar{u}_3), \tag{14}$$

or

$$\frac{\partial^2}{c_3^2 \partial t^2} (\nabla \cdot \bar{u}_3) = \nabla^2 (\nabla \cdot \bar{u}_3) , \tag{15}$$

where

$$c_3^2 = \frac{\lambda_3}{\rho_3}$$

2.1.3 Elastic Constants

An isotropic solid is completely characterized by two elastic constants and its density. A fluid requires one constant in addition to the density. For convenience, the interrelationships between constants are collected here.

Y = Young's modulus
B = Bulk modulus
μ = Shear modulus
σ = Poisson's ratio
λ = Lamé coefficient

The moduli are usually given in units of 10^6 psi. A convenient conversion factor is 1 psi = 6.8948 $(g/cm^3)(m/s)^2$. Often the units given are kg/mm^2, where kg means kg-force. Such values are to be multiplied by 9.8 m/s^2 to obtain the correct units, i.e. 1 kg-force/mm^2 = 9800. $(g/cm^3)(m/s)^2$. Poisson's ratio is dimensionless. The interrelationships are

$$Y = 3B(1 - 2\sigma),$$

$$Y = 2\mu(1 + \sigma),$$

$$\lambda = B - 2\frac{\mu}{3},$$

$$c_1^2 = \frac{\lambda + 2\mu}{\rho_1} \text{ (compressional velocity)},$$

$$c_2^2 = \frac{\mu}{\rho_1} \text{ (shear velocity)}$$

$$c_1^2/c_2^2 = \frac{2(1 - \sigma)}{(1 - 2\sigma)},$$

$$\sigma = \frac{c_1^2 - 2c_2^2}{2\left(c_1^2 - c_2^2\right)}$$

For a fluid one can consider $\mu = 0$ and $\sigma = 1/2$. Using the subscript 3 for the fluid medium:

$$\lambda_3 = B_3$$

$$c_3^2 = \frac{B_3}{\rho_3} \text{ (compressional velocity in fluid)}.$$

In what is to follow, the speeds of sound and densities, ρ, are used as the elastic constants.

2.1.4 Boundary Conditions

The boundary conditions at the interface between medium and

and target are

(1) continuity of normal displacement,

(2) continuity of normal stress,

(3) continuity of tangent shear stress.

These conditions are very general. The first states that the interface does not separate, the others that the interface does not contain any stresses of its own. (The latter conditions would not hold, for example, if surface tension were important, or if the boundary were a thin shell. In these cases, the stresses in the boundary surface would equal the discontinuity in the stresses between medium and target.)

Equating the values of these quantities on inside and outside:

1. $u_{n_3} = u_n$,

2. $\rho_3 c_3^2 \, (\nabla \cdot \bar{u}_3) = \rho_1 c_1^2 \, (\nabla \cdot \bar{u}) - 2\rho_1 c_2^2 \, (\nabla_S \cdot \bar{u})$,

3. $0 = \mu\left(\frac{\partial u_{tan}}{\partial n} + \frac{\partial u_n}{\partial tan}\right)$.

Condition (2) is obtained from the normal diagonal component of Hooke's Law (equation 5), using the relation

$$\frac{\partial u_n}{\partial n} = (\nabla \cdot \bar{u}) - (\nabla_S \cdot \bar{u}).$$

The operator ∇_S contains only surface derivatives. Condition (3) is obtained from the off-diagonal terms in the same row of equation (5).

Additional boundary relations which can be obtained from the above and the equations of motions are

4. $c_3^2 \frac{\partial}{\partial n} (\nabla \cdot \bar{u}_3) = c_1^2 \frac{\partial}{\partial n} (\nabla \cdot \bar{u}) + 2 c_2^2 \nabla_S^2 u_n$.

5. $\frac{\partial}{\partial n} (\hat{n} \cdot \nabla \times \bar{u}) = 0$

where

$\hat{n}$ is the unit normal out of the surface.

Condition (4) is obtained by equating the normal components of the equations of motion (9) and (14) (justified by condition (1)), and by using the relation

$$\hat{n} \cdot \nabla \times (\nabla \times \bar{u}) = \hat{n} \cdot \nabla_S \times (\nabla \times \bar{u}) = -\nabla_S \cdot \hat{n} \times (\nabla \times \bar{u}) = -2 \nabla_S^2 u_n \ . \qquad (16)$$

The last step of the above is from the fact that boundary condition (3) implies that the surface components of the curl can be written in terms of surface derivatives of u_n:

$$\hat{n} \times (\nabla \times \bar{u}) = 2 \nabla_S u_n \ . \qquad (17)$$

Condition (5) can be derived through use of condition (3).

It is to be noted that the boundary conditions also hold under differentiation by t and directional differentiation in the surface (∇_S). Also note that by equation (14) and B.C. (1):

$$\ddot{u}_n = c_3^2 \frac{\partial}{\partial n} (\nabla \cdot \bar{u}_3) \qquad (18)$$

For a fluid target these boundary conditions are simplified by the facts that $c_2 = 0$ and that condition (3) does not apply (or rather, is satisfied trivially by the fact that $\mu = 0$). We thus have, for a fluid target in a fluid medium:

1. $u_{n_3} = u_n$

2. $\rho_3 c_3^2 \, (\nabla \cdot \bar{u}_3) = \rho_1 c_1^2 \, (\nabla \cdot \bar{u})$

4. $c_3^2 \frac{\partial}{\partial n} (\nabla \cdot \bar{u}_3) = c_1^2 \frac{\partial}{\partial n} (\nabla \cdot \bar{u})$

In addition, $(\nabla \times \bar{u})$ is identically zero in a fluid.

As a further degeneracy, consider sound-hard and soft targets, for which no acoustic energy penetrates the target, i.e., $\nabla \cdot \bar{u}$ is also identically zero. A sound-hard target can be considered as the extreme case where $\rho_1 \to \infty$; hence we obtain the boundary condition

$$\ddot{u}_n = c_3^2 \frac{\partial}{\partial n} (\nabla \cdot \bar{u}_3) = 0 \ ,$$

and only $(\nabla \cdot \bar{u}_3)$ is free to vary. A sound-soft target can be considered as the other extreme where $\rho_1 \to 0$, so that

$$\nabla \cdot \bar{u}_3 = 0$$

and only $\ddot{u}_n$ is free to vary.

2.1.5 Relations Between Displacement and Pressure

In an ideal fluid there are no shear stresses and Hooke's Law reduces to

$$P^e = -B(\nabla \cdot \bar{u}_3) \ ,$$

or

$$P^e = -c_3^2 \rho_3 (\nabla \cdot \bar{u}_3), \tag{19}$$

where P^e is the excess pressure. The minus sign is introduced since $(\nabla \cdot \bar{u})$ is the change in volume/unit volume, which is negative for an increase in pressure.

At the surface

$$\frac{\partial P^e}{\partial n} = -c_3^2 \rho_3 \frac{\partial}{\partial n} (\nabla \cdot \bar{u}_3) = -\rho_3 \ddot{u}_n \ . \tag{20}$$

Hence in the fluid, the displacement can be interpreted directly in terms of excess pressure.

2.2 INTEGRAL EQUATION SOLUTION

2.2.1 STIE For Scattered and Interior Waves

Using the Green's function $G(\bar{r}|\bar{r}', t|\tau) = \frac{1}{R} \delta(\tau - R/c_3 - t)$, where $R = \bar{r} - \bar{r}'$, a solution to the wave equation can be developed, known as the Kirchoff integral representation:

$$\nabla \cdot \bar{u}_3(\bar{r},t) = \left(\nabla \cdot \bar{u}_3(\bar{r},t)\right)^{inc} - \frac{1}{4\pi} \int_S \frac{1}{R} \frac{\partial}{\partial n'} (\nabla \cdot \bar{u}_3') dS' + \frac{1}{4\pi} \int_S (\hat{n}' \cdot \hat{R}) L_3 (\nabla \cdot \bar{u}_3') dS'$$

(21)

where the integrals are over the bounding surface,

$\hat{n}'$ is the unit normal out of the surface,

R is the magnitude of $\bar{R} = \bar{r} - \bar{r}'$,

$\hat{R}$ is the unit direction of $\bar{R}$,

$$L_3 = \frac{1}{R^2} + \frac{1}{c_3 R} \frac{\partial}{\partial \tau} ,$$

$$(\nabla \cdot \bar{u}_3') = \nabla \cdot \bar{u}_3(\bar{r}', \tau) \text{ , with } \tau = t - R/c_3 .$$

$(\nabla \cdot u_3)^{inc}$ is due to sources external to the surface (the incident pressure).

The above is for the exterior wave. Maintaining the convention that $\hat{n}$ points out of the surface, for the interior waves, the sign of the integrals is changed and there is no incident term. Hence:

$$\nabla \cdot \bar{u}(\bar{r},t) = \frac{1}{4\pi} \int_S \frac{1}{R} \frac{\partial}{\partial n'} (\nabla \cdot \bar{u}') dS' - \frac{1}{4\pi} \int_S (\hat{n}' \cdot \hat{R}) \, L_1 (\nabla \cdot \bar{u}') dS' \qquad (22)$$

and

$$\nabla \times \bar{u}(\bar{r},t) = \frac{1}{4\pi} \int_S \frac{1}{R} \frac{\partial}{\partial n'} (\nabla \times \bar{u}') dS' - \frac{1}{4\pi} \int_S (\hat{n}' \cdot \hat{R}) \, L_2 (\nabla \times \bar{u}') dS' \qquad (23)$$

Here, L_1, L_2, $(\nabla \cdot u')$, etc. are defined analogously to the quantities in equation (21). Note that the retardation is $t - \tau = R/c_1$ in equation (22) and $t - \tau = R/c_2$ in equation (23).

2.2.2 STIE on Boundary

To solve the scattering problem, these equations are first solved on the boundary, after which the scattered field may be obtained from equation (21). To obtain the solution on the surface, the observation

point, $\bar{r}$, is moved to the surface and a limiting process applied. The result is the following set of integral equations for $\bar{r}$ on the surface:

$$\nabla \cdot \bar{u}_3(\bar{r},t) = 2\left(\nabla \cdot \bar{u}_3(\bar{r},t)\right)^{inc} - \frac{1}{2\pi} \int \frac{1}{R} \frac{\partial}{\partial \vec{n}} (\nabla \cdot \bar{u}_3') dS'$$

$$+ \frac{1}{2\pi} \int (\hat{n}' \cdot \hat{R})\ L_3(\nabla \cdot \bar{u}_3') dS' \qquad (24)$$

$$\nabla \cdot \bar{u}(\bar{r},t) = \frac{1}{2\pi} \int \frac{1}{R} \frac{\partial}{\partial \vec{n}} (\nabla \cdot \bar{u}') dS' - \frac{1}{2\pi} \int (\hat{n}' \cdot \hat{R})\ L_1(\nabla \cdot \bar{u}') dS' \qquad (25)$$

$$\nabla \times \bar{u}(\bar{r},t) = \frac{1}{2\pi} \int \frac{1}{R} \frac{\partial}{\partial \vec{n}} (\nabla \times \bar{u}') dS' - \frac{1}{2\pi} \int (\hat{n}' \cdot \hat{R})\ L_2(\nabla \times \bar{u}') dS' \qquad (26)$$

To solve the above, the integrals are replaced by summations over finite patches, over which R and the field variable are assumed constant. The "self-patch" contribution (which includes the point $\bar{r}$) is integrated analytically. For the first term of the integral over the self-patch at $\bar{r}_k$, we define

$$\gamma_k = \frac{1}{2\pi} \int_{\Delta S_k} \frac{dS'}{R} = \sqrt{\frac{\Delta S_k}{\pi}} \qquad (27)$$

For the second term, we represent $\nabla \cdot \bar{u}_3'$ by a Taylor expansion about $\bar{r}$:

$$\nabla \cdot \bar{u}_3' = \nabla \cdot \bar{u}_3 + \rho\left(\frac{\partial}{\partial x} (\nabla \cdot \bar{u}_3) \cos\theta + \frac{\partial}{\partial y} (\nabla \cdot \bar{u}_3) \sin\theta - \frac{\partial}{c_3 \partial t} (\nabla \cdot \bar{u}_3)\right)$$

and $\hat{n}'$ by

$$\hat{n}' = \hat{n} - \rho(K_1 \hat{x} \cos\theta + K_2 \hat{y} \sin\theta)\ ,$$

where

K_1, K_2 are the principal curvatures,

x, y is the surface (curvilinear) coordinate system, $dS' = \rho d\rho d\theta$.

The second integral over the self-patch then becomes $\varepsilon_k(\nabla \cdot \bar{u}_3)$,

where

$$\varepsilon_k = \gamma_k\left(\frac{K_1 + K_2}{2}\right) \tag{28}$$

We then can write

$$\left.\begin{aligned}
&(1-\varepsilon_k)(\nabla \cdot \bar{u}_3)_k + \gamma_k \frac{\partial}{\partial n}(\nabla \cdot \bar{u}_3)_k = -I_{3k} + 2(\nabla \cdot \bar{u}_3)_k^{inc} \\
&(1+\varepsilon_k)(\nabla \cdot \bar{u})_k - \gamma_k \frac{\partial}{\partial n}(\nabla \cdot \bar{u})_k = I_{1k} \\
&(1+\varepsilon_k)(\nabla \times \bar{u})_k - \gamma_k \frac{\partial}{\partial n}(\nabla \times \bar{u})_k = \bar{I}_{2k}
\end{aligned}\right\} \tag{29}$$

where

$$I_{3k} = \sum_{j \neq k} \frac{\Delta S_j}{2\pi}\left\{\frac{\partial}{\partial n'}(\nabla \cdot \bar{u}_3')_j - L_{3j}(\nabla \cdot \bar{u}_3')_j(\hat{n}_j' \cdot \hat{R}_{jk})\right\}$$

with similar expressions for I_{1k} and $\bar{I}_{2k}$ (the "non-self integrals").

The discrete formulations of the non-self integrals contain ten quantities: $\nabla \cdot \bar{u}_3$, $\nabla \cdot \bar{u}$, $\nabla \times \bar{u}$ and their normal derivatives at retarded times. One quantity is identically zero (B.C. 5), so that 9 quantities need to be stored at all space and time sample points to evaluate the integrals. If the time step is chosen sufficiently small so that the retardation is always greater than a time step, the solution can proceed by a straightforward process of marching in time.

2.2.3 Simultaneous Solution of STIE on Boundary

At each space-time point, equations (29) need to be solved simultaneously for the 9 quantities of interest. This is done by application of the boundary conditions. Using B.C. 2 and 4, the first two equations can be rewritten (suppressing the subscript k):

$$(1-\varepsilon)(\nabla\cdot\bar{u}_3) + \gamma\frac{\partial}{\partial n}(\nabla\cdot\bar{u}_3) = 2(\nabla\cdot\bar{u}_3)^{inc} - I_3$$

$$\beta(1+\varepsilon)(\nabla\cdot\bar{u}_3) - \gamma\frac{\partial}{\partial n}(\nabla\cdot\bar{u}_3) = I_1 - \alpha\left((1+\varepsilon)(\nabla_S\cdot\bar{u}) + \gamma\nabla_S^2 u_n\right) \tag{30}$$

Here we have used the relations

$$(\nabla\cdot\bar{u}) = \beta(\nabla\cdot\bar{u}_3) + \alpha(\nabla_s\cdot\bar{u})$$

$$\frac{\partial}{\partial n}(\nabla\cdot\bar{u}) = \frac{c_3^2}{c_1^2}\frac{\partial}{\partial n}(\nabla\cdot\bar{u}_3) - \alpha\nabla_s^2 u_n\,, \tag{31}$$

where

$$\beta = \frac{\rho_3 c_3^2}{\rho_1 c_1^2}$$

$$\alpha = 2\,c_2^2/c_1^2$$

This pair of equations can be solved for $(\nabla \cdot \bar{u}_3)$ and its normal derivative, if the displacement vector $\bar{u}$ is known at time t over the entire surface. Since from (18),

$$\frac{\partial^2 u_n}{\partial t^2} = \frac{1}{c_3^2} \frac{\partial}{\partial n} (\nabla \cdot \bar{u}_3) ,$$

u_n can be found from earlier values by the relation

$$u_n(t) = 2\, u_n(t - \Delta t) - u_n(t - 2\,\Delta t) + (\Delta t)^2 \frac{\partial^2 u_n}{\partial t^2} (t - \Delta t). \qquad (32)$$

The surface components of $\bar{u}$ can be found by numerical solution of the interior wave equation (9). For example, if $\hat{a}_1$ and $\hat{a}_2$ are orthogonal directions in the surface and u_1 is $\hat{a}_1$ component of $\bar{u}$, etc:

$$\frac{\partial^2 u_1}{\partial t^2} = c_1^2 \frac{\partial}{\partial a_1} (\nabla \cdot \bar{u}) + c_2^2 \left[\frac{\partial}{\partial n} (\nabla \times \bar{u})_{a_2} - \frac{\partial}{\partial a_2} (\nabla \times \bar{u})_n \right]. \qquad (33)$$

Since $\partial/\partial n\ (\nabla \times \bar{u})_n = 0$, the normal component of the last of equations (29) yields directly

$$(\nabla \times \bar{u})_n = \frac{1}{(1 + \varepsilon)} (\bar{I}_2 \cdot \hat{n}) . \qquad (34)$$

Surface differentiation then yields the third term in equation (33). Now the surface components of $(\nabla \times \bar{u})$ can be obtained, by virtue of B.C. 3, from equation (17). Hence the surface components of the last of equations (29) yields

$$\frac{\partial}{\partial n} (\nabla \times \bar{u})_{a_2} = \frac{(1 + \varepsilon)}{\gamma} (\nabla \times \bar{u})_{a_2} - \frac{1}{\gamma} (\bar{I}_2 \cdot \hat{a}_2) , \qquad (35)$$

with a similar expression for the $\hat{a}_1$ component. Hence u_1 and u_2, in the surface, can be found by equation (33) from earlier values in time by application of a relation similar to equation (32).

The solution is now complete. It can be seen to require three integrations over the retarded field values on the boundary, one integration for each kind of wave (exterior, interior compressional, interior shear), where each wave is associated with its own retardation. It also appears that 9 quantities need to be stored at all time and space points. Although these quantities are related by the boundary conditions, it is computationally advantageous to store them all, rather then recomputing them when required to evaluate the STIE.

2.2.4 Incident Field

The incident pressure is taken as a plane wave with time dependence

$$(\nabla \cdot \vec{u})^{inc} = \frac{a_n}{\sqrt{\pi}} e^{-(a_n t)^2} , \qquad (36)$$

the "smoothed impulse". The calculation is started at a time such that the incident field is still very small at the closest point: $(a_n t) \approx 3$.

In the frequency domain, the smoothed impulse has the same shape, with appreciable amplitude out to $k \approx \pi a_n$. The frequency response of the target could thus be obtained, by convolution, from 0 to $k \approx \pi a_n$. Since larger a_n requires smaller time and space steps for solution accuracy, practical considerations (computer storage and running time), limit a_n to 1 or 2.

For the computations of a target on the bottom (see Section 2.4) a nearby source was taken, which includes a 1/R dependence. The amplitude

of this spherical wave was normalized such that if the source were located at ∞ on a hard bottom, the result would be the incident field of equation (36). For nearby source:

$$p^{inc} = \frac{a_n R_s}{2\sqrt{\pi}} \left[\frac{e^{-(a_n t_1)^2}}{R_1} \pm \frac{e^{-(a_n t_2)^2}}{R_2} \right] \tag{37}$$

where

+ is for the hard bottom,

- is for the soft bottom,

R_s = distance from source to target center,

R_1 = distance from source to target point,

R_2 = distance from image source to target point,

$t_1 = t + R_s - R_1$,

$t_2 = t + R_s - R_2$.

2.2.5 Scattered Field

The scattered pressure, p^e, or equivalently $(\nabla \cdot \bar{u}_3)$, is given by equation (21) of Section 2.2.1; repeated here

$$\nabla \cdot \bar{u}_3(\bar{r},t) = -\frac{1}{4\pi} \int_S \frac{1}{R} \frac{\partial}{\partial n'} (\nabla \cdot \bar{u}_3') \, dS' + \frac{1}{4\pi} \int_S (\hat{n}' \cdot \hat{R}) L_3 (\nabla \cdot \bar{u}_3') \, dS' \tag{38}$$

which is valid in the near and far field. That is, of all the quantities computed on the surface, only two: $(\nabla \cdot \bar{u}_3)$ and $\partial/\partial n \, (\nabla \cdot \bar{u}_3) = 1/c_3^2 \, \partial^2 u_n / \partial t^2$, need to be retained for the scattered pressure calculation.

In the limit as $\bar{r}$ becomes large the above becomes

$$r\left(\nabla \cdot \bar{u}_3(\bar{r},t)\right) = \frac{1}{4\pi} \int_S \left\{ - \frac{1}{c_3^2} \frac{\partial^2 u_n'}{\partial t^2} + (\hat{n}' \cdot \hat{r}) \frac{1}{c_3} \frac{\partial}{\partial t} (\nabla \cdot \bar{u}_3') \right\} dS' \qquad (39)$$

Note that the (bistatic) response can be calculated for any observation direction without recalculating the surface quantities; the latter are associated with a particular direction of incidence. The near field evaluation of (38) was done for the case of targets on the bottom.

2.3 REDUCTION OF ELASTIC SCATTERING PROBLEM TO SIMPLER CASES

It is instructive to see how these equations reduce to simpler forms for simpler problems.

2.3.1 Fluid Target

For example, consider the fluid-fluid problem, for which the target does not support shear waves. For this case, the constants μ and c_2 are zero, and there is no equation (23). Boundary condition (3) does not apply and boundary conditions (2) and (4) are simplified by the loss of exactly those terms ($\nabla_S \cdot \bar{u}$ and $\nabla_S^2 u_n$) which required the numerical solution of the wave equations in the elastic problem. Equation (29) can thus be solved directly, using boundary relations (2) and (4). The retarded integration requires storage of only 2 quantities in all space time. Also, using relation (19), the equations can be written in terms of the excess pressure P^e and its normal derivative $\partial P/\partial n$. Equation (24) for pressure on the surface, then becomes

$$P(\bar{r},t) = 2P^{inc}(\bar{r},t) - \frac{1}{2\pi} \int \frac{1}{R} \frac{\partial}{\partial n'} P' \, dS' + \frac{1}{2\pi} \int L_3 \, P'(\hat{n}' \cdot \hat{R}) dS' \, . \qquad (40)$$

Equation (25) can be similarly reformulated.

2.3.2 Hard and Soft Targets

If no acoustic energy penetrates the targets, equation (25) also disappears and we are left simply with (21) or (40). The boundary conditions for this case are either that the target is perfectly rigid (sound-hard) for which $\partial p/\partial n = 0$, or that the target is a pressure-release surface (sound-soft) at which $p = 0$. For both cases, one of the integrals in (40) disappears. The solution thus requires only one space-time integration over the retarded boundary value and requires the storage of only one quantity in space-time. This is the problem which has been solved at the Sperry Research Center for a variety of geometrical configurations [9,10,11].

2.4 TARGET IN THE PRESENCE OF A BOTTOM

We consider here the case of perfectly hard or soft targets; that is, equation (40) applies with the condition that either $\partial p/\partial n = 0$ (sound-soft) or $p = 0$ (sound hard). After solving analytically for the "self-patch", this equation is rewritten as

$$p(\bar{r},t) = \frac{1}{(1-\varepsilon)} \left[2\, p^{inc}(\bar{r},t) + \frac{1}{2\pi} \int_{NS} (\hat{R}\cdot\hat{n}')L_3\, p'\, dS' \right] \qquad (41)$$

for the sound-hard target; or as

$$\frac{\partial p}{\partial n}(\bar{r},t) = \frac{1}{\gamma} \left[2\, p^{inc}(\bar{r},t) - \frac{1}{2\pi} \int_{NS} \frac{1}{R} \frac{\partial}{\partial n'} p'\, dS' \right] \qquad (42)$$

for the sound-soft target, where the integrals are over the non-self part of the surface and γ, ε, L_3 are defined in Section 2.2.2.

If a sound-hard or soft plane near the target is added to the scattering problem, rather than solving (41) or (42) on the plane, a method of images is applied.

2.4.1 Method of Images

We assume again that the plane bottom is either perfectly hard or perfectly soft. That is, we have one of equations (41) or (42) on the bottom. Also assuming that the plane is ∞, we see in Fig. 3 that the boundary conditions on the plane are satisfied if we remove the bottom and add symmetrically placed targets and sources below the bottom plane. This latter configuration has the same pressure field in the upper half-space as does the original configuration. In the case of a hard bottom, the reflected source has the same sign as the original source; and in the case of a soft bottom, the reflected source must be of opposite sign to satisfy the boundary condition on the plane.

We note that by symmetry the value of the pressure (or its normal derivative) at a point on the image target is the same as that at the symmetric point on the original target (with a + or - sign, respectively, for a hard or soft bottom). In the numerical calculation we therefore do not calculate the image pressure explicitly, although its contribution to the pressure at a target point is, of course, included in the summation of equations (41) and (42). Also, in equations (41) and (42), we understand p^{inc} to mean the total incident pressure wave from the source and its image (see Section 2.2.4). We can then apply these equations without further change.

Note that in the case of a sound-soft bottom, the effect of the source and its image tend to cancel at a point on the target. The pressure at the target is due to the difference in path length from the two sources - the closer the source is to the bottom, the smaller is the target surface pressure until the source hits the bottom, which is equivalent to no source at all and the pressure is zero everywhere.

In the case of a sound-hard bottom, an interesting case is that for which a target (symmetrically shaped) is half-penetrating the bottom with the source located on the bottom (see Fig. 3c). This case is equivalent

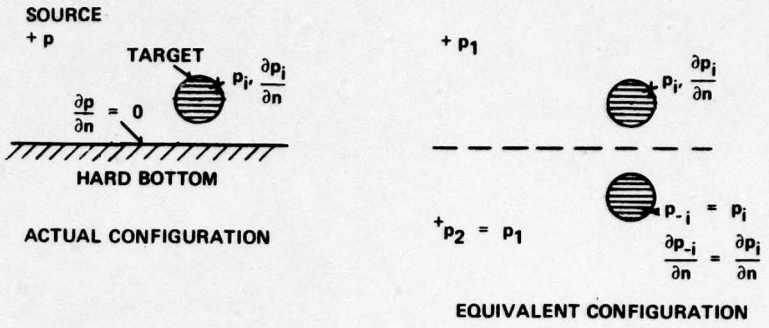

(a) SOUND-HARD BOTTOM

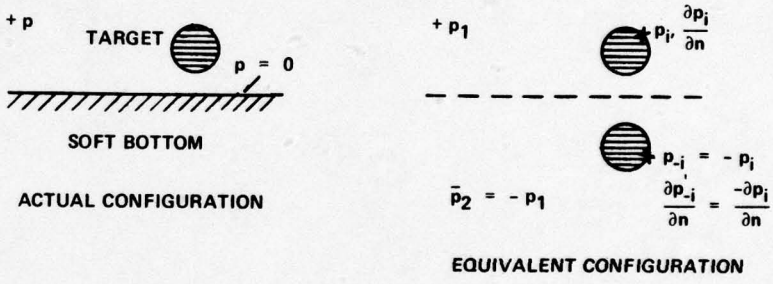

(b) SOUND-SOFT BOTTOM

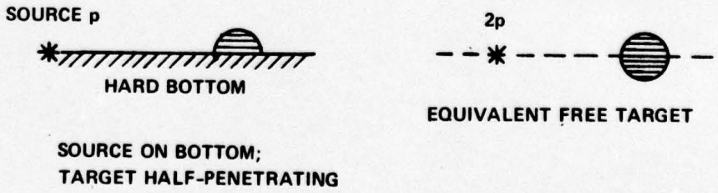

(c) FREE TARGET EQUIVALENT

78-161

FIG. 3 Method of images.

to the target in free space with double the strength of the source. This configuration (with the source moved far away) was used to check the new program ECHOB by comparison with the existing program ECHO for free targets.

2.4.2 Self-Term Integration for Patches Close to Bottom

As has been discussed, the non-self integrals in the STIE are evaluated numerically by dividing the target into a number of patches and assuming constant values of R and p or $\partial p/\partial n$ over a patch. This becomes inaccurate when R is small, which occurs in particular when the integration point, $\bar{r}'$, is the image of the observation point, $\bar{r}$, and $\bar{r}$ is close to the bottom. This happens, for example, when a sphere or cylinder lies tangentially to the bottom. This problem is handled by integrating such patches analytically. The result of the image patch integration is included in the expression for γ or ε and the integrals (41) and (42) are understood to omit this patch. The result depends on whether the bottom is hard or soft.

For a hard target on a hard bottom:

$$\varepsilon_H = \varepsilon\left(1 + \sqrt{1 + (2z/\gamma)^2} - (2z/\gamma)\right) - \left(n_z - z\frac{(K_1 + K_2)}{2}\right)\left(1 - \frac{(2z/\gamma)}{\sqrt{1 + (2z/\gamma)^2}}\right); \tag{43a}$$

for a hard target on a soft bottom:

$$\varepsilon_s = \varepsilon\left(1 - \sqrt{1 + (2z/\gamma)^2} + (2z/\gamma)\right) + \left(n_z - z\frac{(K_1 + K_2)}{2}\right)\left(1 - \frac{(2z/\gamma)}{\sqrt{1 + (2z/\gamma)^2}}\right). \tag{43b}$$

For a soft target on a hard bottom:

$$\gamma_H = \gamma\left(1 + \sqrt{1 + (2z/\gamma)^2} - (2z/\gamma)\right) \tag{44a}$$

for a soft target on a soft bottom:

$$\gamma_s = \gamma\left(1 - \sqrt{1 + (2z/\gamma)^2} + (2z/\gamma)\right) \tag{44b}$$

where z is the distance of the patch center from the bottom, n_z is the component of the target normal in the direction of negative bottom normal, K_1, K_2 are the principal curvatures of the patch. These expressions are derived in reference [10].

SECTION 3
NUMERICAL SOLUTION

3.1 REPRESENTATION OF THE TARGET

The surface of the target is represented by a set of more or less uniformly spaced nodes. Each node is associated with an area ("patch") and is defined by position $\bar{r}$, normal $\hat{n}$, principal curvatures K_1, K_2, and directions of principal curvature $\hat{a}_1$, $\hat{a}_2$, where $\hat{n} = \hat{a}_1 \times \hat{a}_2$. For a target rotationally symmetric about the z-axis, $\hat{a}_2$ is taken as lying along the generating curve (or meridian) and $\hat{a}_1 = \hat{\phi}$ (Fig. 4). These quantities are pregenerated and stored for each node by the geometry section of the computer program, (with the vectors represented in the cartesian coordinate system).

The target is centered at the origin and the incident field direction is taken to lie in the z-y plane. A larger number of nodes increases the accuracy of solution, but is limited by computation time ($\sim N^2$) and computer storage requirements ($\sim N$). Node spacings as large as 0.4 (or $\sim$ 90 nodes on a sphere) have been found to be adequate for uniform meshes. For long thin targets (such as the cylinder) a non-uniform mesh can be used, with higher node concentration at regions of high curvature (or near edges) where the field is expected to change most rapidly.

3.2 NUMERICAL REPRESENTATION OF THE STIE

In Section 2.2.2 the STIE's were integrated analytically over the self-patch. For discrete time and space points this is written (at time t_j at point $\bar{r}_k$):

$$(1 - \varepsilon_k)\left(\nabla \cdot \bar{u}_3(t_j)\right)_k + \gamma_k \frac{\partial}{\partial n}\left(\nabla \cdot \bar{u}_3(t_j)\right)_k = 2\left(\nabla \cdot u_3(t_j)\right)^{inc} - I_{3NS_k} \qquad (45)$$

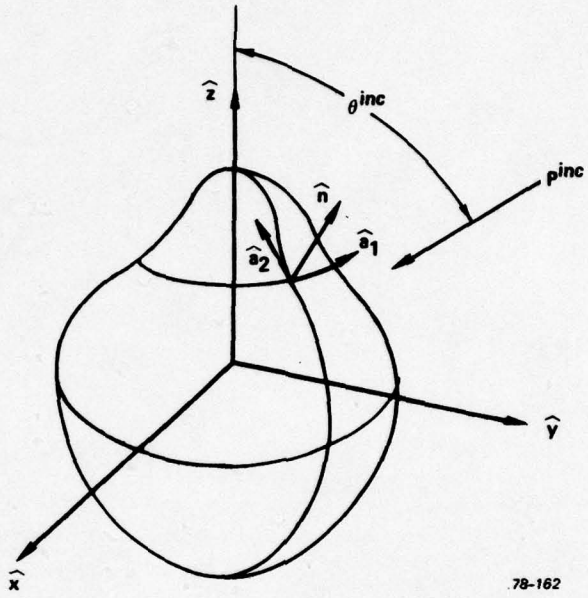

FIG. 4 Target geometry.

where

$$I_{3NS_k} = \frac{1}{2\pi} \sum_{\ell \neq k} \left\{ \frac{1}{R_{k\ell}} \frac{\partial}{\partial n} \left(\nabla \cdot \bar{u}_3(\tau_{jk\ell}) \right)_\ell - (\hat{R}_{k\ell} \cdot \hat{n}_\ell) \; L_3 \left(\nabla \cdot \bar{u}_3(\tau_{jk\ell}) \right)_\ell \right\} \Delta S_\ell \; , \tag{46}$$

$$\tau_{jk\ell} = t_j - R_{k\ell}/c_3 \; ,$$

$$L_3 = \frac{1}{R_{k\ell}^2} + \frac{1}{R_{k\ell} c_3} \frac{\partial}{\partial \tau}$$

Similar forms are written for $(\nabla \cdot \bar{u})$ and $(\nabla \times \bar{u})$.

If the time step, Δt, is taken sufficiently small so that $R_{k\ell}/c_3 > \Delta t$ for all $(k\ell)$, then the field values in the non-self integrals are strictly retarded. Hence the non-self integrals can be evaluated at time t_j from the field values at earlier times. It is thus necessary to store the nine quantities that appear in the integrals for each node and for all time points from the current time back to the time corresponding to the greatest retardation. For efficient use of computer storage this required time window is stepped along with the stepping in t_j. The size of the time window is given by

$$T_W = R_{max}/c_{min} \; , \tag{47}$$

where R_{max} is the maximum distance between any two nodes and c_{min} is the minimum of c_1, c_2, c_3. The evaluation of the field quantities at time τ is done by interpolation on the discreet values.

The non-self integral for the curl equation is a vector: Each contribution to the sum is evaluated in the local coordinate system of the integration point, ℓ, then transformed to the coordinate system of the observation point, k, to permit the vector addition of the contributions. The values of the displacement vector $\bar{u}$ at all nodes is also stored

for the current and previous time point.

The solution procedure can now be summarized: at time t,

(1) Evaluate the three non-self integrals (2 scalar and one vector equation), using the retarded values of the nine field quantities, $(\nabla \cdot \bar{u}_3)$, $(\nabla \cdot \bar{u})$, $(\nabla \times \bar{u})$, and their normal derivatives.

(2) Evaluate $(\nabla_s^2 u_n)$ and $(\nabla_s \cdot \bar{u})$ by numerical differentiation in the surface, using the current value of $\bar{u}$.

(3) Solve the first two equations of (29) for $(\nabla \cdot \bar{u}_3)$ and $\partial/\partial n\ (\nabla \cdot \bar{u}_3)$ at the current time point and find $(\nabla \cdot \bar{u})$ and $\partial/\partial n\ (\nabla \cdot \bar{u})$ by the relations (31).

(4) Evaluate the normal component of $(\nabla \times \bar{u})$ from the normal part of the vector STIE (equation 34).

(5) Evaluate the surface components of $(\nabla \times \bar{u})$ by numerical differentiation of u_n in the surface, using equation (17).

(6) Use the relation (35) to find the surface components of $\partial/\partial n\ (\nabla \times \bar{u})$. (The normal component is identically 0.)

(7) Use the result of (3) and (4) to find the surface derivatives of $(\nabla \cdot \bar{u})$ and $(\nabla \times \bar{u})_n$.

(8) From the relation (33) evaluate the surface components of $\partial^2 \bar{u}/\partial t^2$.

(9) Obtain $\bar{u}$ at the next time point $(t + \Delta t)$, by numerical extrapolation (equation 32).

The process is now repeated for the next time point.

Strictly speaking, since the nine field quantities are related by the boundary conditions, not all need to be stored to evaluate the non-self integrals. In fact, it can be argued that the problem is fully *described by only* 4 quantities (and their derivatives). It was found to be more efficient and accurate, however, to retain all 9 field variables. An alternate approach is described in the Appendix.

3.3 SURFACE DERIVATIVES

An important step in the above procedure is the evaluation of derivatives in the surface. It should be noted that these derivatives do not appear in the degenerate cases of fluid, hard, and soft targets, so that the elastic problem represents a large increase in complexity, requiring the evaluation of a vector integral as well as surface differentiation.

A convenient way to form these derivatives is to consider a plane tangent to the surface at the node k and then projecting the adjacent nodes and the vector $\bar{u}$ at those nodes upon the plane. A second order Taylor expansion of $\bar{u}$ is written about node k, e.g. for u_n:

$$u_n(\ell) = u_n(k) + \frac{\partial u_n}{\partial a_1}(\Delta a_1) + \frac{\partial u_n}{\partial a_2}(\Delta a_2) + \frac{\partial^2 u_n}{\partial a_1^2}\frac{(\Delta a_1)^2}{2} + \frac{\partial^2 u_n}{\partial a_2^2}\frac{(\Delta a_2)^2}{2}$$

$$+ \frac{\partial^2 u_n}{\partial a_1 \partial a_2}(\Delta a_1)(\Delta a_2) \qquad (48)$$

As there are generally 6 adjacent nodes in addition to the node k itself, the above can be solved for the derivatives by a least square fit. This fitting process needs to be performed only once and the result put into the form of a 6 x 7 matrix, S. The derivatives are then evaluated when required by

$$[D] = S[u_n] \qquad (49)$$

where [D] is the column of derivative values at node k and $[u_n]$ is the column of values of u_n at k and the adjacent nodes. One matrix S and the indices of the adjacent nodes are stored for each node.

The advantage of this process is that the evaluation of the STIE becomes independent of the geometrical representation of the target. In

particular, nodes do not have to be placed along coordinate lines as required by the usual finite difference techniques.

For problems with special geometries, such as a sphere, the derivatives may be written in the curvilinear coordinate system and evaluated using their finite difference representations, rather than using the plain projection method above. For the first order derivatives the two approaches give similar results; the second order derivatives, however, can be different. As discussed later, at the present time the problem of accurate determination of second surface derivates has not been resolved and appears to be the cause of instabilities in the solution procedure.

3.4 SYMMETRY RELATIONS

To increase the efficiency of the solution, symmetry conditions are used whenever possible. Scattering at arbitrary angles of incidence from a rotationally symmetric target has plane symmetry (Fig. 4). The symmetry plane is taken as the $x = 0$ plane. The field quantities are calculated and stored only for nodes at $x \geq 0$ and their values at $x < 0$ inferred from the symmetry conditions.

The values of the scalar quantities $(\nabla \cdot \bar{u})$, etc. at $(-x)$ are the same as at (x). For the vector quantities the following table summarizes the symmetry conditions, where - indicates a sign reversal upon reflection in the $x = 0$ plane

Vector	Components					
	$\hat{n}$	$\hat{a}_1$	$\hat{a}_2$	$\hat{x}$	$\hat{y}$	$\hat{z}$
$\bar{u}$	+	-	+	-	+	+
$\nabla \times \bar{u}$	-	+	-	+	-	-

(50)

[Recall (Fig. 4) that $\hat{a}_1$ is identified with $\hat{\phi}$, $\hat{a}_2$ is in the direction of increasing z and $\hat{n}$ is the outward normal.]

For a rotationally symmetric problem, i.e. axial incidence upon a rotationally symmetric target, the symmetry conditions are even more restrictive. We then have that the scalar quantities are constant under rotation about the axis of symmetry. The vector quantities, in our curvilinear coordinate system, rotate along with the target rotation, hence the items marked "-" in the table on the preceding page are required to be 0 for the rotationally symmetric problem:

Vector	Components		
	$\hat{n}$	$\hat{a}_1$	$\hat{a}_2$
$\bar{u}$	.	0	.
$(\nabla \times \bar{u})$	0	.	0

3.5 INSTABILITY PROBLEMS

Most of the instability problems that arise in the STIE solution have been solved; one problem, that of a stable formulation of surface derivatives, remains.

3.5.1 Types of Instabilities

Three classes of instabilities have been identified, which may be named, suggestive of their origin: time-, space-, and resonance instabilities.

The time-like instability is affected strongly by the time step of the solution, setting in rapidly when the time step is too large. The onset of this instability is made later by taking a time step smaller than the time required for a wave to propagate between adjacent nodes,

$$\Delta t \leq R_{min}/c_{max} \quad . \tag{52}$$

Reducing the time step further does not affect the stability appreciably. The nature of this instability is rapid oscillations which build up in amplitude very rapidly and are in phase on the surface. The calculated far field response is smooth up to some point near the end when it suddenly breaks up with rapidly increasing oscillations. This problem does not occur for the perfectly hard target, probably because the nearest patches do not contribute heavily to the non-self integral (since there is no $\partial p/\partial n$ term. This problem is completely eliminated by including some smoothing in the time interpolation performed in the evaluation of the retarded contributions to the non-self integral. The time interpolation is performed to second order on the values at the three time points closest to the time τ; these three values however are obtained by linear smoothing of the nearest five time points. This process eliminates the instabilities as they arise and also yields continuous first derivatives as required. (Linear interpolation gives rise to another instability due to discontinuity in the first derivates; higher order interpolation does not provide sufficient smoothing.)

The space-like instability appears to be caused by the discrete representation of the target geometry. It appears as an inaccuracy at some critical point (the specular point or edges) and is then propagated with slowly increasing amplitude over the surface. Oscillations on the surface are in phase.) The period of oscillation is slower and corresponds to the target size. The size of the time step only affects the phase but not the magnitude of this instability. This problem can be eliminated by modeling the target with a finer mesh near the critical points. A finer mesh, by relation (52), also requires a smaller time step, which may not be practical for large targets. To keep the time-step large (i.e. only small enough to satisfy (52) for most nodes) an iterative procedure was developed, which is applied to the nodes in the fine part of the mesh:

First, the non-self integrals are evaluated at all nodes, omitting the contributions from the nearby nodes. Then the contributions from the nearby nodes are added, including in the interpolation procedure the newly calculated field values at the current time points. One repetition of the last step gives sufficiently good results. The use of a local fine mesh and iterative solution has eliminated this instability in the case of hard and soft targets. At time of writing, this procedure has not been included in the elastic solution, partly in order to minimize complexity at this initial stage and partly because other instability problems were felt to be more severe.

A third type of instability can be identified, named the resonance instability, which appears to be caused by an interaction of the discrete formulation of space and time points. This instability is not in phase on the surface and is not necessarily oscillatory (at some nodes the field amplitude may increase exponentially). It shows up in the far field calculation as an exponentially increasing response. This problem has not been solved, but it appears only for certain unfortunate choices of time step. Slight increases or decreases in the time step can eliminate this instability.

3.5.2 Surface Derivative Instabilities

The remaining instability problem appears only in the general elastic calculation. It has the nature of a space-like instability, indicating that it is due to the inaccurate determination of some quantity, which error is then propagated with amplification over the surface. As can be seen in the results presented in the next section, this error appears in the far field response as a slow oscillation of increasing amplitude. This problem is particularly severe because its onset is at the beginning of time. This problem has not been solved. The likely cause is the determination of the surface derivatives, in particular of the term $\nabla_s^2 u_n$. It should be noted that the surface derivates are taken, not of

quantities determined directly by the STIE, but of $\bar{u}$ which is obtained by numerical integration of $\partial^2\bar{u}/\partial t^2$. This process is another source of inaccuracy. Proposals for solving this instability problem include the use of the iterative solution in conjunction with a finer mesh, and the formulation of the problem with finite-element techniques which would avoid the need for space derivatives.

3.6 THE ANALYTIC SOLUTION FOR A SPHERE

The eigenvalue solution of scattering from an elastic sphere was implemented in order to test the STIE solution and to provide another means of analyzing the measured data. This solution proceeds by writing the eigenfunction expansions of the three waves and solving for the coefficients by application of the boundary conditions. The result is a very complicated expression for the coefficients, which will not be duplicated here, but is given in [1] and [2]. The solution (far field response) is written in terms of frequency. It is given by straightforward evaluation of the coefficients and of the Bessel and Hankel functions of the scattered wave expansion.

This solution was also used to examine the nature of the response as a function of elastic parameters.

3.7 CONVOLUTION PROCEDURE

It is often necessary to compare responses in the frequency domain, or to compare responses with different inputs. A convolution procedure accomplishes this.

Let e(t) be the input signal given at discrete time points, and r(t) the discrete response. Then the complex frequency response of the target is given by

$$H(\omega) = R(\omega)/E(\omega) \ , \tag{53}$$

where $E(\omega) = F\left(r(t)\right)$, the discrete FFT, and where the division represents the discrete (complex) division of R by E at corresponding values of ω.

The time domain response to a different input $e'(t)$ can then be calculated by forming

$$r'(t) = F^{-1}\left(H(\omega) \cdot F\left(e'(t)\right)\right) ,$$

where F^{-1} is the inverse discrete FFT. Of course, $H(\omega)$ and $r'(t)$ are valid only over the band over which $E(\omega)$ is defined. The magnitude of H is plotted in the results to follow.

3.8 SCALING

It is convenient to present the target response in a form independent of scattering geometry and medium parameters. Therefore we write:

time in units of ct/a
frequency in units of $ka = 2\pi fa/c$
scattered pressure in units $r_o p/a$ per unit incident pressure.

Here

c is the medium speed of sound,
a is a typical target dimension (radius for the sphere and cylinder
r_o is the distance of the target from the observation point.

The frequency response H(ka), as calculated in Section 3.7, is then independent of incident wave form and amplitude, observation distance, target size, and elastic properties of the medium. The only quantities of importance then are target shape and the ratios of target density and sound velocities to those of the medium.

[It is to be noted, that the scaling given above differs from the commonly used "reflectivity". The latter is defined as σ/cross-sectional

area, where σ is the "cross-section" or cross-sectional area of an equivalent sphere. The power reflected is then $\sigma/4\pi r_o^2$ or $\pi a^2/4\pi r_o^2 = (a/2r_o)^2$ for the sphere. That is, whereas the reflectivity is 1 (at high frequency) for a sphere, our scaled response is 1/2.]

SECTION 4
COMPUTATIONAL RESULTS

In this section we first give the results of analysis of elastic sphere responses based on the analytic solution. This will be followed by a summary of results of STIE calculations for the elastic and fluid sphere and cylinder, and of hard and soft cylinders near or on a bottom.

4.1 ANALYTIC RESULTS FOR A SPHERE - EFFECTS OF ELASTIC PARAMETERS

In Fig. 5 are presented the responses in the frequency domain of aluminum and brass spheres. The elastic constants used are

	c_1 (m/s)	c_2 (m/s)	ρ (g/cm^3)
Aluminum 6061-T6	6180	3090	2.706
Naval Brass	4400	2100	8.394
Medium	$c_3 = 1490$	-	1.026

Also shown in Fig. 5 are the responses of hard and soft spheres. Figure 6 illustrates the same responses in the time domain, for a smoothed impulse with $a_n = 1$. A feature shared by all responses are the resonances at intervals of $\delta(ka) = 1.22$, which are characteristic of the size of the sphere. This phenomenon is due to the existence of creep waves. The creep wave path length is longer than that of the specular return by $(2 + \pi)a$, hence the creep wave is reinforcing if $(2 + \pi)a = n\lambda = \frac{2\pi n}{k}$, (for n integer), or $ka = 1.222\ n$. Correspondingly, in the time domain we observe a response at $\delta(ct/a) = 2 + \pi$ after the specular return.

A feature distinctive of the elastic solid response is the existence of deep nulls in the response. We observe that these nulls are spaced at about $\delta(ka) = 2.4$ for aluminum and at $\delta(ka) = 1.6$ for brass, which is approximately in the ratio of the shear velocities of the two materials.

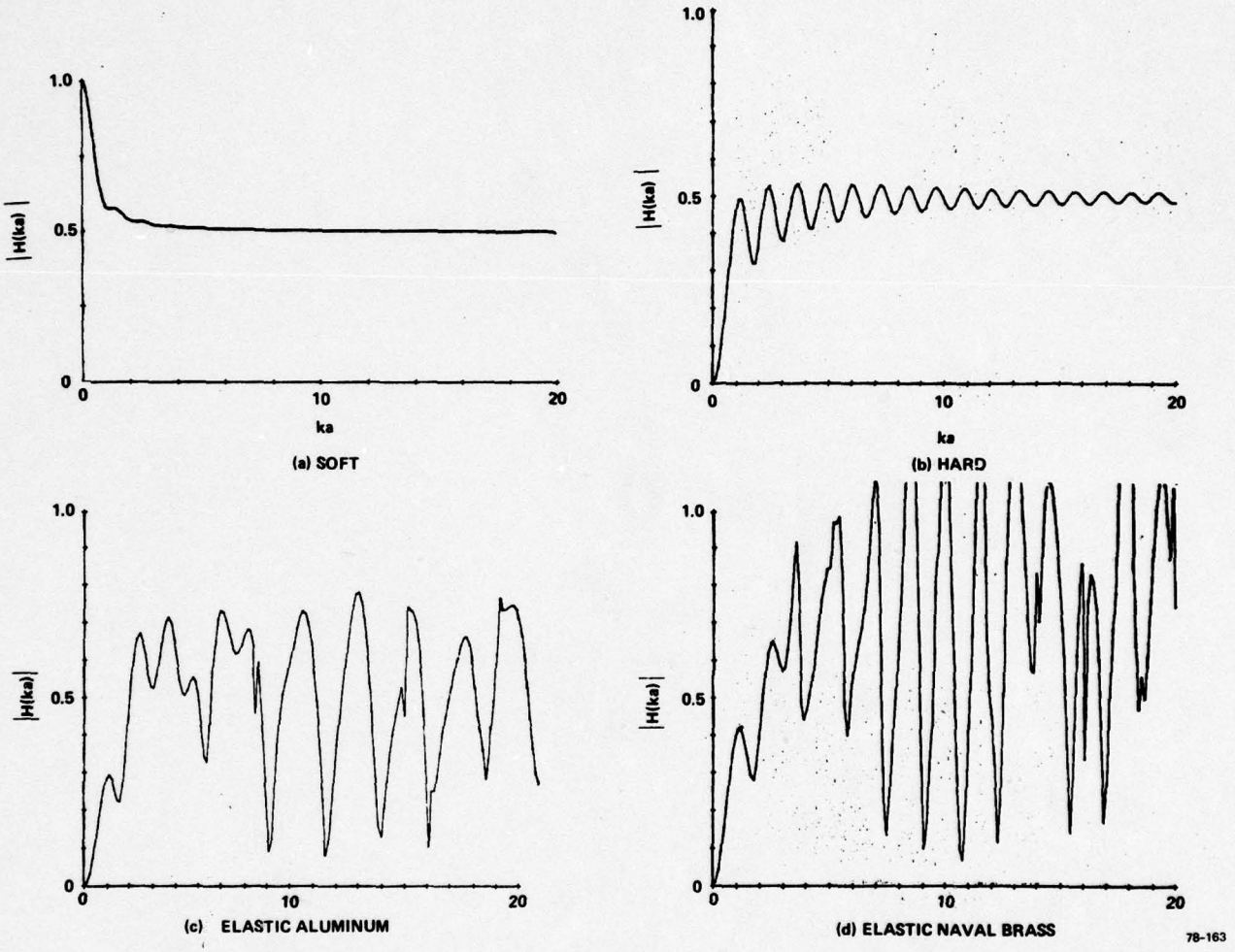

FIG. 5 Frequency response – soft, hard, elastic spheres.

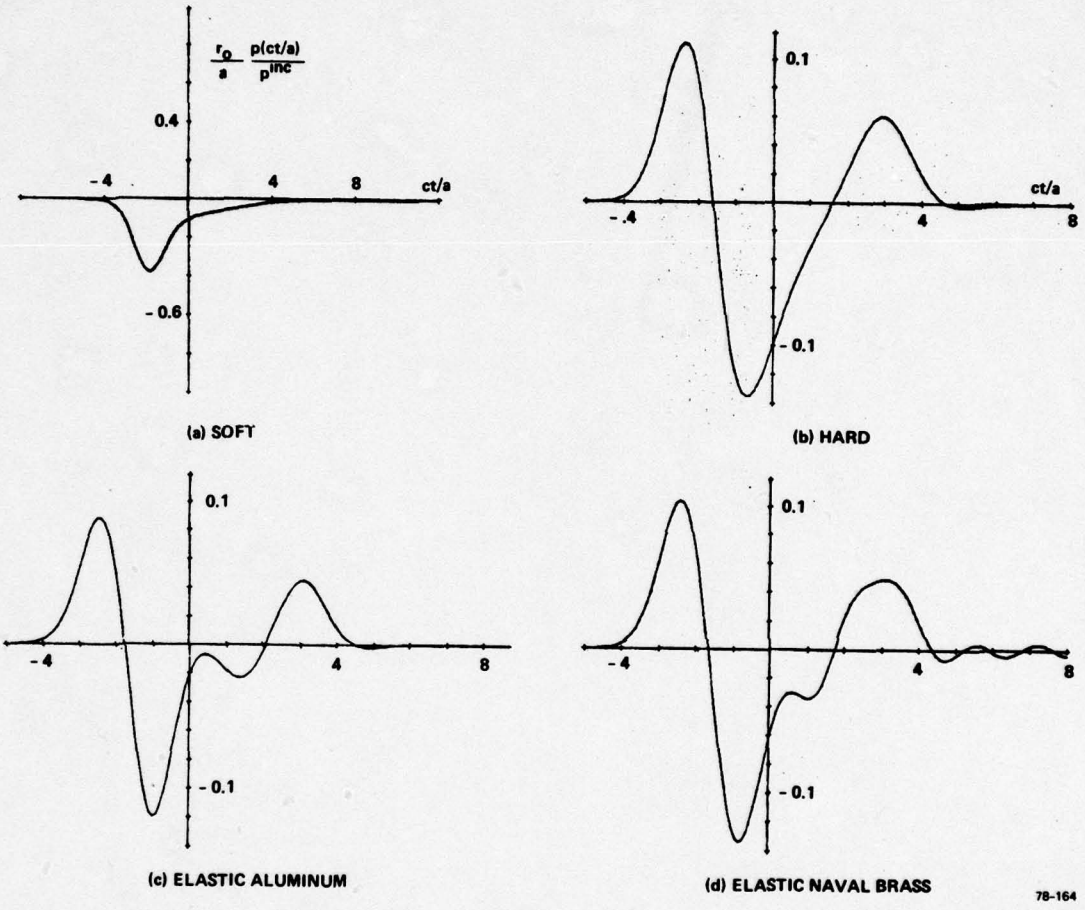

FIG. 6 Smoothed impulse response – soft, hard, elastic spheres.

It is difficult to interpret these resonances. They correspond approximately to the difference in time traversal from the point at $\theta = 45°$ to $-45°$ around the back of the sphere. That is, a creep wave at the shear velocity. The 45° point is where from physical considerations we expect the largest coupling into the shear wave. In the time domain, for aluminum, the above $\delta(ka) = 2.4$ corresponds to $\delta(ct/a) = 2.6$, and indeed a response is seen at that interval after the specular return. However, the corresponding shear creep return is not observed for brass ($\delta(ct/a) = 3.9$). For brass in the time domain we observe a wiggle at about $\delta(ct/a) = 2.9$ after the specular return. This corresponds approximately to the delay of a shear wave starting at $\theta = 45°$, traversing the sphere through the center, reflecting from $-135°$ and coupling out at $-45°$. We also note that the initial, specular, return is not much lower in amplitude for the hard and these elastic targets. That is, not much acoustic energy is coupled into the interior compressional wave. This is probably the reason that a return due the interior compressional wave, which has reflected from the back side, is not apparent (it would show up at $\delta(ct/a) = 1$ for aluminum).

To illustrate the effect of the elastic parameters on the response, we compare the aluminum response with that of materials with different shear velocities c_2 but the same ρ_1 and c_1 (Figs. 7 and 8). We see that the specular part of the return is changed but little, as might be expected since there is little coupling into a shear wave near the specular point. The main change is in the amplitude of the wiggle after $t = 0$, which is thus clearly associated with the shear wave. In Figs. 9 and 10 is shown the effect of a change in ρ_1 and the effect of a change in c_1, keeping the other two parameters the same as for aluminum.

4.2 STIE RESULTS FOR ELASTIC AND FLUID TARGETS

The computational results for a sphere using the STIE formulation is given in Fig. 11 for aluminum and in Fig. 12 for brass. These are the smoothed impulse responses. Also shown are the calculated hard

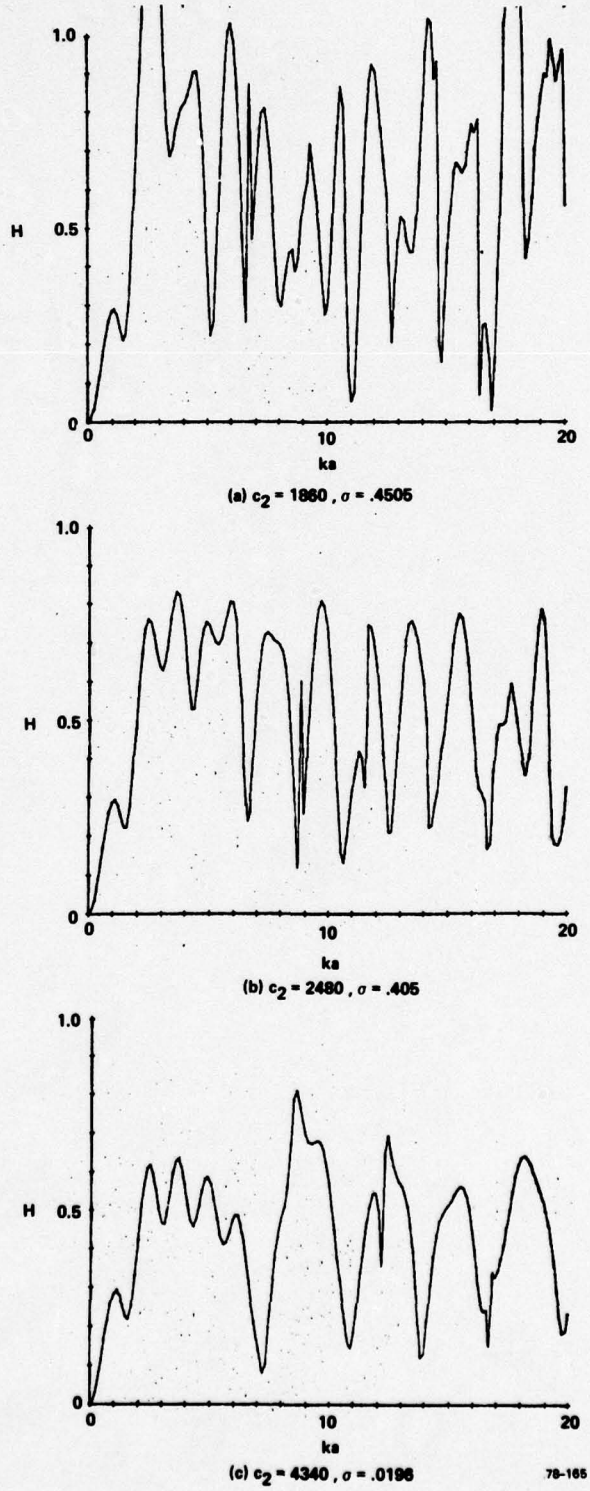

FIG. 7 Effect of shear velocity c_2 on frequency response of sphere. Medium: c = 1480, ρ = 1; target: c_1 = 6200, ρ_1 = 2.7.

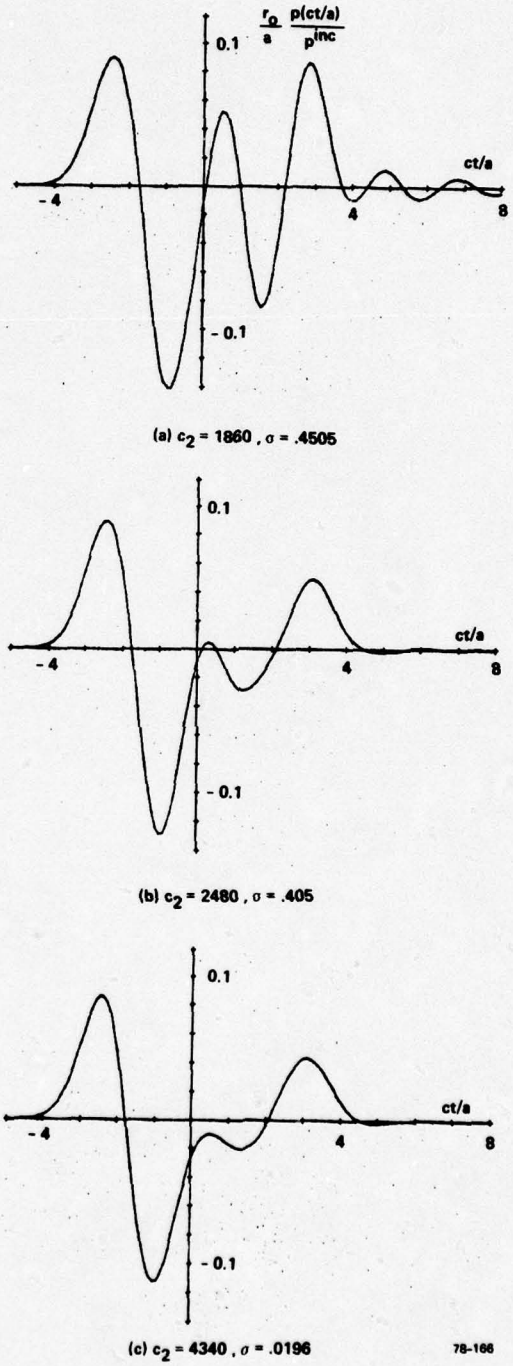

FIG. 8 Effect of shear velocity c_2 on smoothed impulse response of sphere.

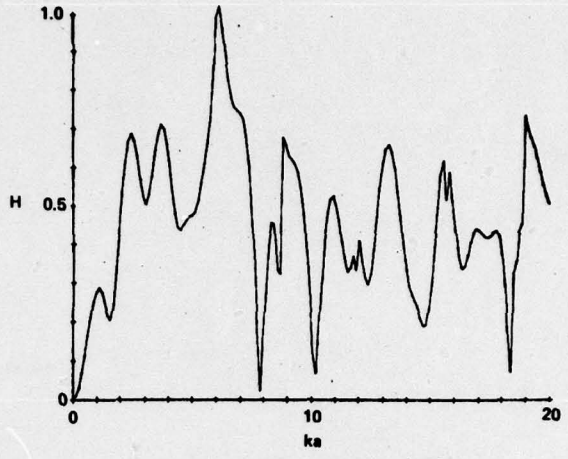

(a) $\rho_1 = 2.7$, $c_1 = 4430$, $\sigma = .0202$

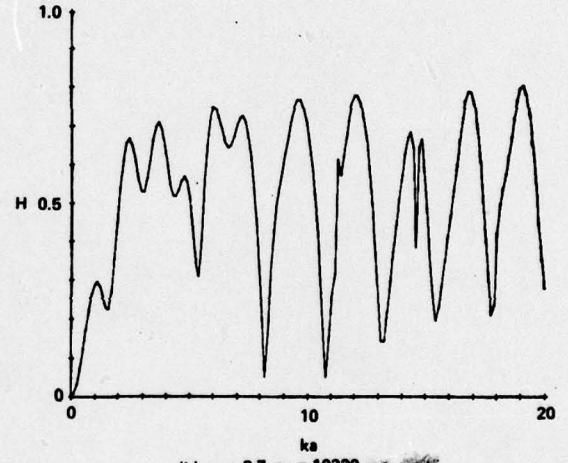

(b) $\rho_1 = 2.7$, $c_1 = 10330$, σ = [illegible]

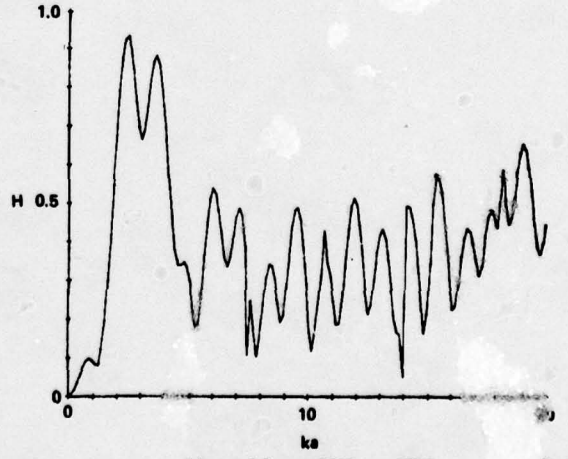

(c) $\rho_1 = 1.0$, $c_1 = 6200$, $\sigma = .3333$ 78-167

FIG. 9 Effect of compressional velocity c_1 and density ρ_1 on frequency response of sphere. Medium: $c = 1480$, $\rho = 1$; target: $c_2 = 3100$.

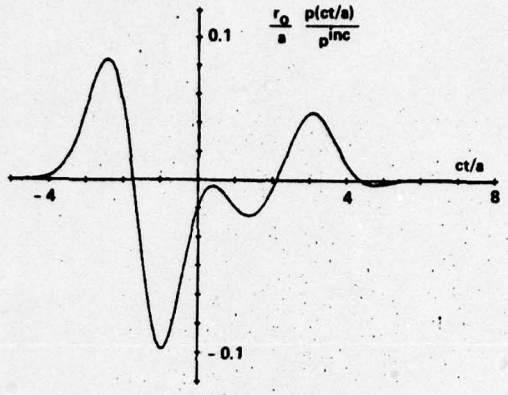

(a) $\rho_1 = 2.7$, $c_1 = 4430$, $\sigma = .0202$

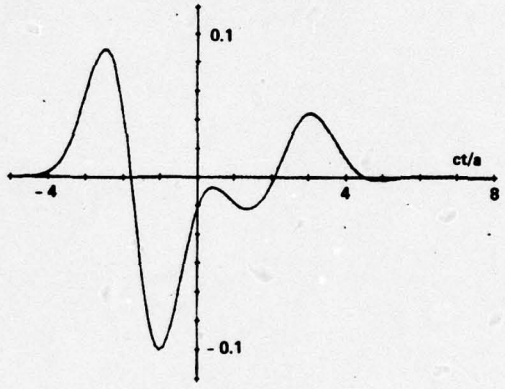

(b) $\rho_1 = 2.7$, $c_1 = 10330$, $\sigma = .4505$

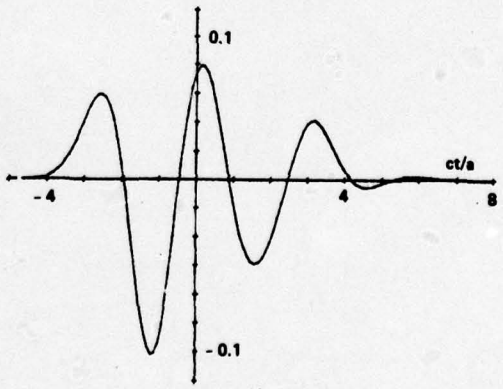

(c) $\rho_1 = 1.0$, $c_1 = 6200$, $\sigma = .3333$ 78-168

FIG. 10 Effect of compressional velocity c_1 and density ρ_1 on smoothed impulse response of sphere. Medium: $c = 1480$, $\rho = 1$; target: $c_2 = 3100$.

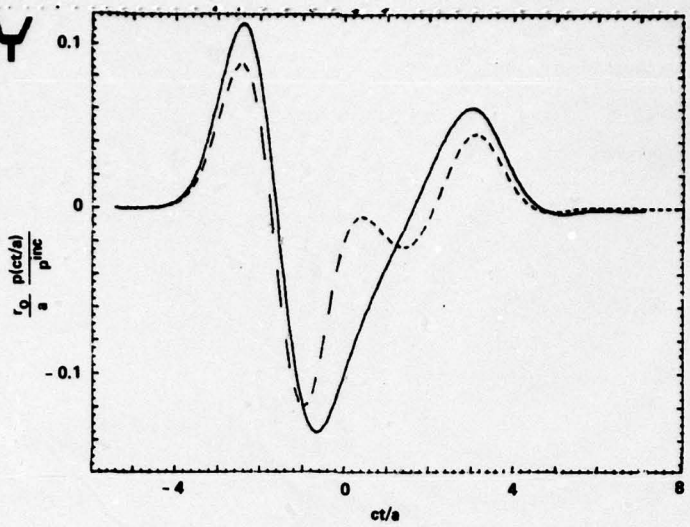

(a) HARD

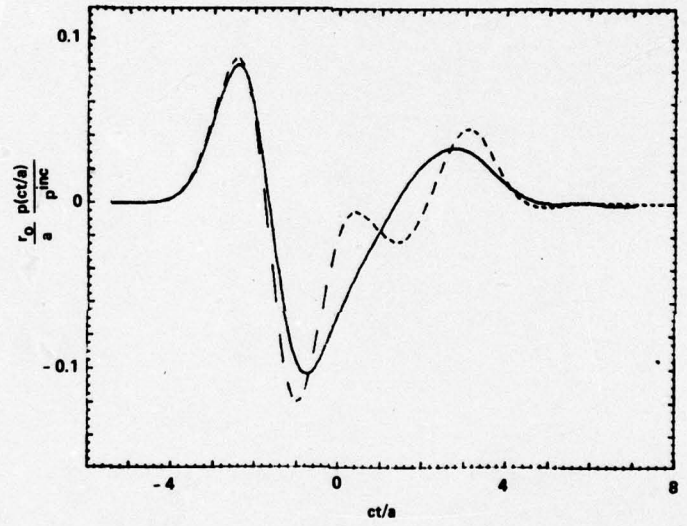

(b) FLUID

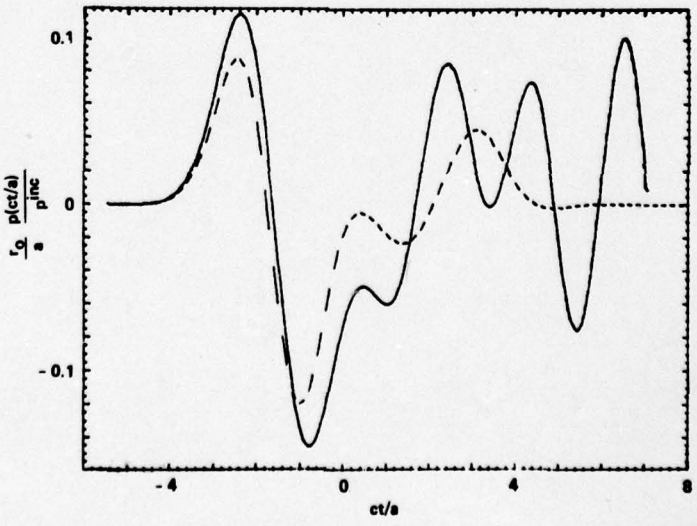

(c) ELASTIC ALUMINUM 78-169

FIG. 11 STIE solution – aluminum sphere (dashed curve is theoretical response).

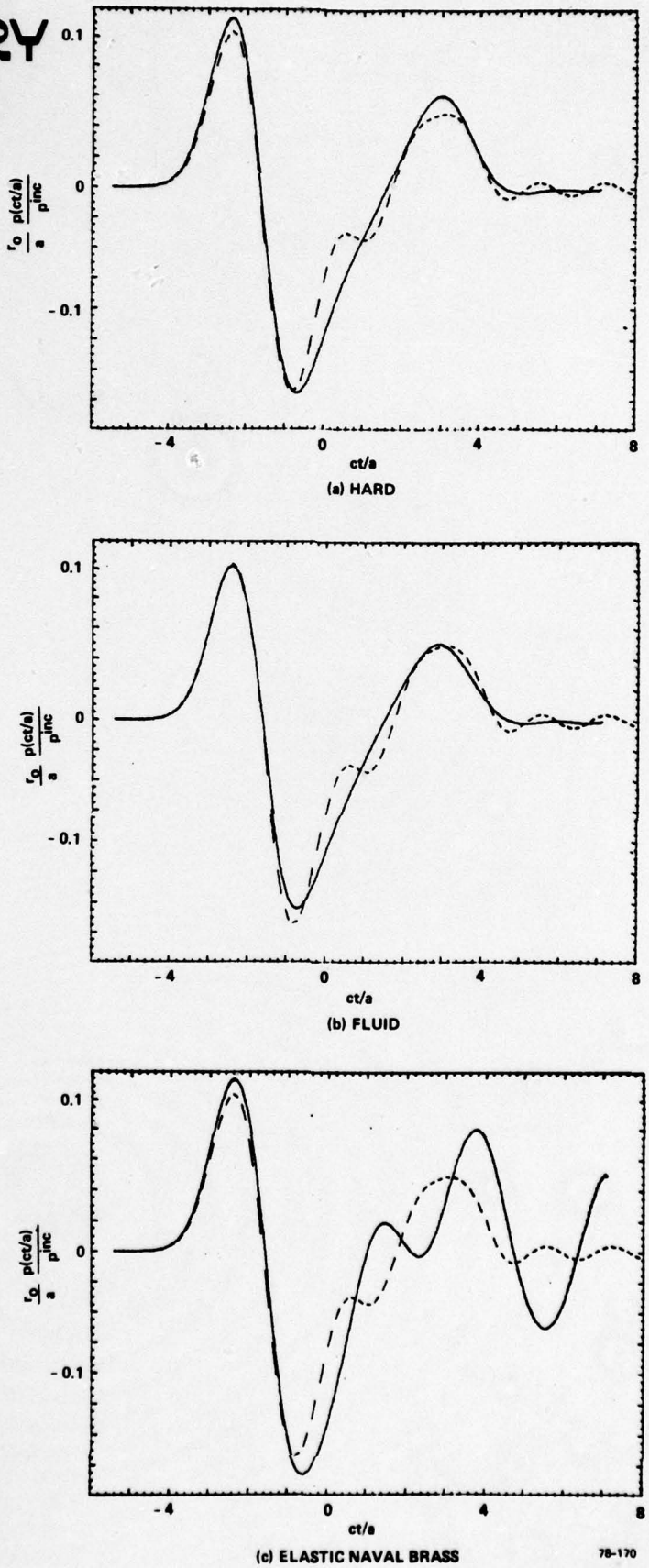

FIG. 12 STIE solution – naval brass sphere (dashed curve is theoretical response).

target and fluid target responses. The calculated hard target response agrees with analytic results to within a few percent. The fluid response is for a target with the same density and compressional wave velocity, but with no shear wave. No theoretical response is available for comparison, but it can be inferred to be correct on the basis of the considerations of the previous section and comparison with the results in ref. [12]. The results for the elastic target are compared with the theoretical result (dotted lines) and illustrate the remaining difficulty with the elastic solution as discussed in Section 3.5.2.

The calculated response of a fluid cylinder at axial incidence is given in Figs. 13 & 14. This is for a cylinder with $L/a = 2$, for aluminum and brass. Superposed on the plots is the hard target response (dotted line). As is the case for the sphere, the fluidity only changes the amplitude of the response.

4.3 STIE RESULTS - TARGETS ON BOTTOM

We present here the smoothed impulse response of several geometries: the sphere and right-circular cylinder at several depths of penetration into the bottom and above the bottom. These calculations were made for sound-hard and sound-soft targets on sound-hard or -soft bottoms. In each case we compare the response with that of a target in free water. In all cases the smoothed impulse width constant is $a_n = 1$; that is, the pulsewidth (at the 1.5% points) is $4/a_n = 4$. The target size is comparable to this pulsewidth - all spheres and cylinders considered here have a diameter of 2, with the cylinder length/diameter = 3/1. The observation point in all cases is the same as the source point, namely $r_o = 10$ and $z = 2$ (height above bottom).

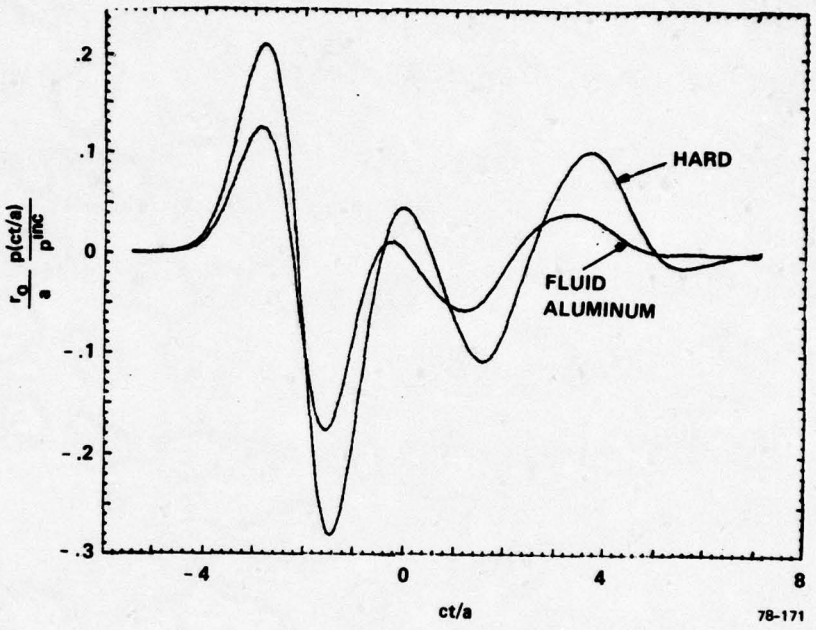

FIG. 13 STIE solution – aluminum RCC (L/a = 2/1), axial incidence (fluid model).

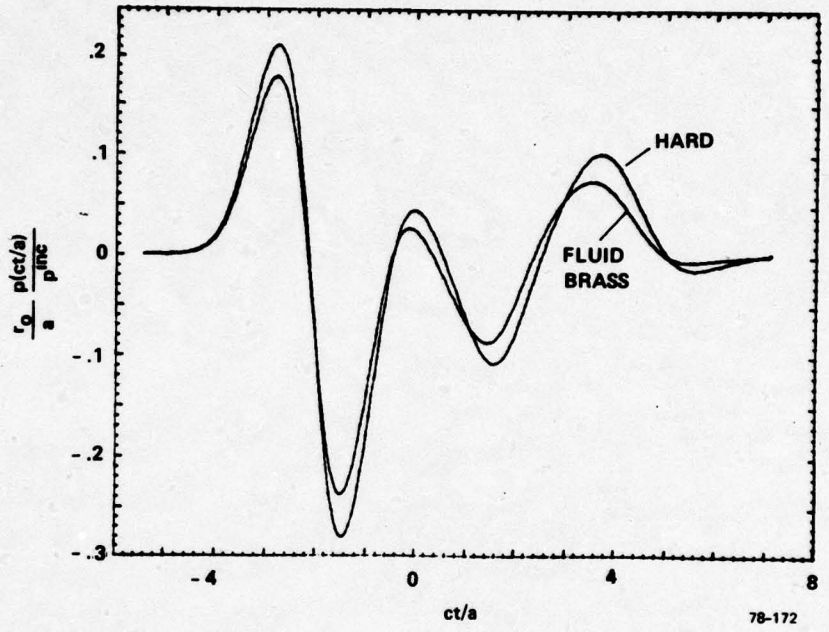

FIG. 14 STIE solution — naval brass RCC (L/a = 2/1), axial incidence (fluid model).

4.3.1 Spheres Near a Flat Bottom

In Fig. 15 we plot the response of hard spheres at several elevations with respect to a hard bottom. The vertical scale differs for each plot so that the shapes may be more readily compared. Superposed on each plot is the response of a free target at the correct relative amplitude.

We identify the initial positive pulse as the specular return and the second positive pulse as the creeping wave. Note that the shapes of all the responses are almost identical to the response of a free target - only the response from a sphere 3/4 embedded in the bottom (case 5) has a creeping-wave to specular-return ratio that is appreciably different from the others. The amplitude of the response shows a simple variation with height above the bottom: increasing as the target approaches the bottom and decreasing again as the target penetrates the bottom.

In Fig. 16 the response of soft spheres near a hard bottom is plotted. Similar to the hard sphere, the effect of the bottom on the soft sphere response is mainly on the amplitude. An exception to this observation is the positive backswing for targets which are entirely above the bottom (case 1 of Fig. 16).

For a soft bottom, the source and its image have opposite signs. The scattered pressure is thus a difference of two similar signals, the net signal being due to the differences in path length associated with each. We thus expect the return from a target near a soft bottom to look somewhat like a derivative of the free target return. This is borne out in Figs. 17 and 18 which show the response of hard and soft targets, respectively, for various elevations of the target with respect to the soft bottom. In comparison with the hard-bottom case, the soft-bottom returns are quite complicated. The signals show an extra peak with additional structure in

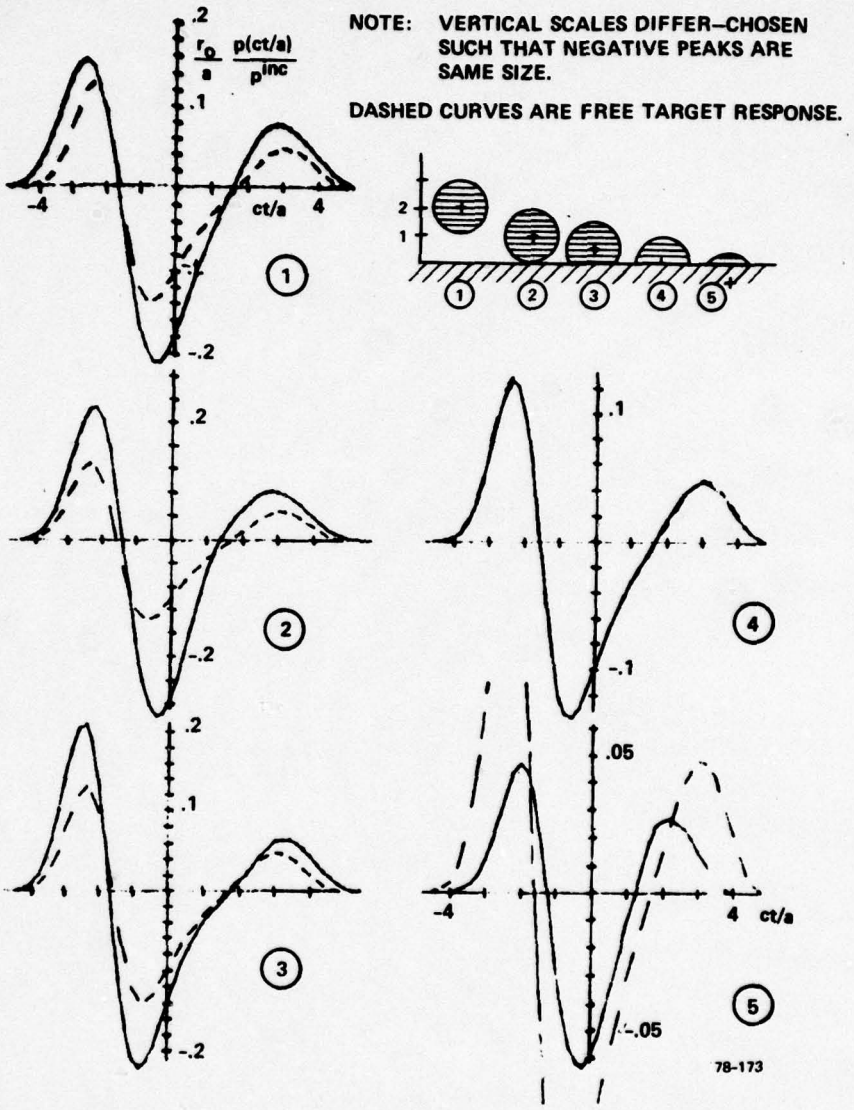

FIG. 15 Smoothed impulse response at various elevations – hard sphere, hard bottom.

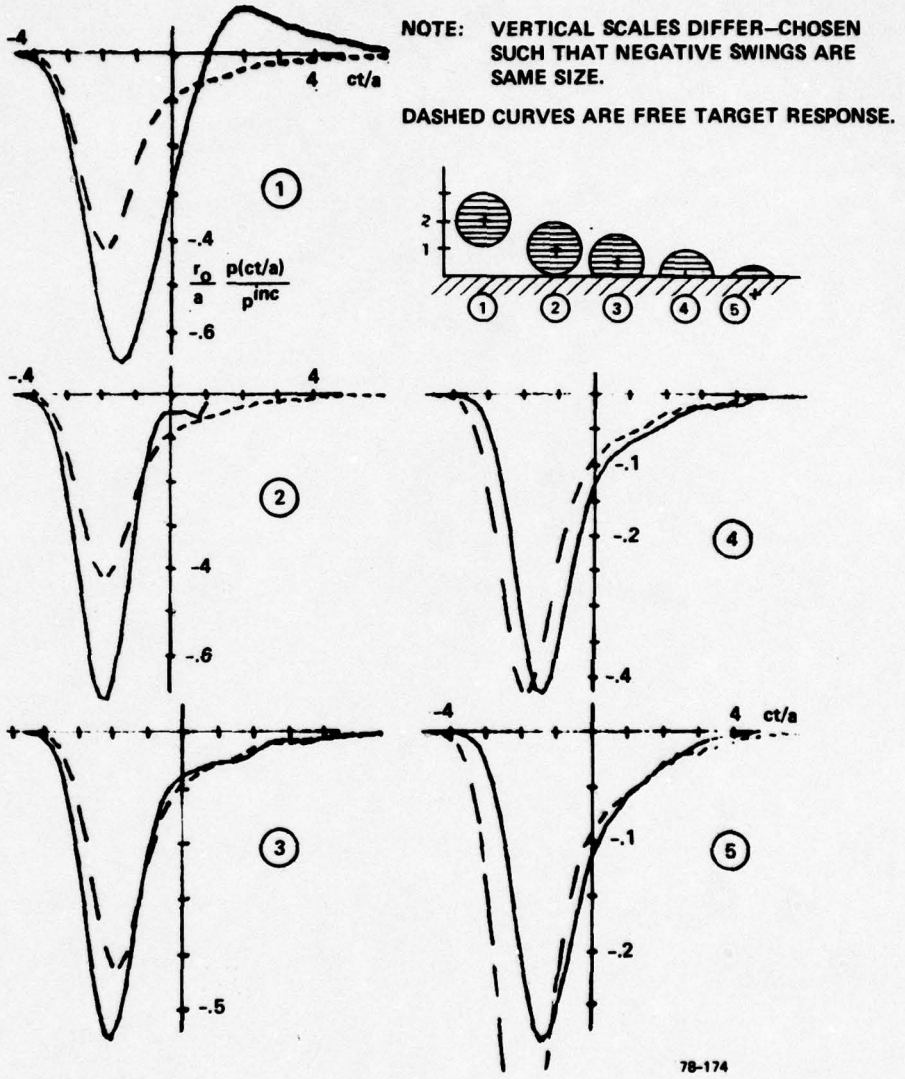

FIG. 16 Smoothed impulse response at various elevations – soft sphere, hard bottom.

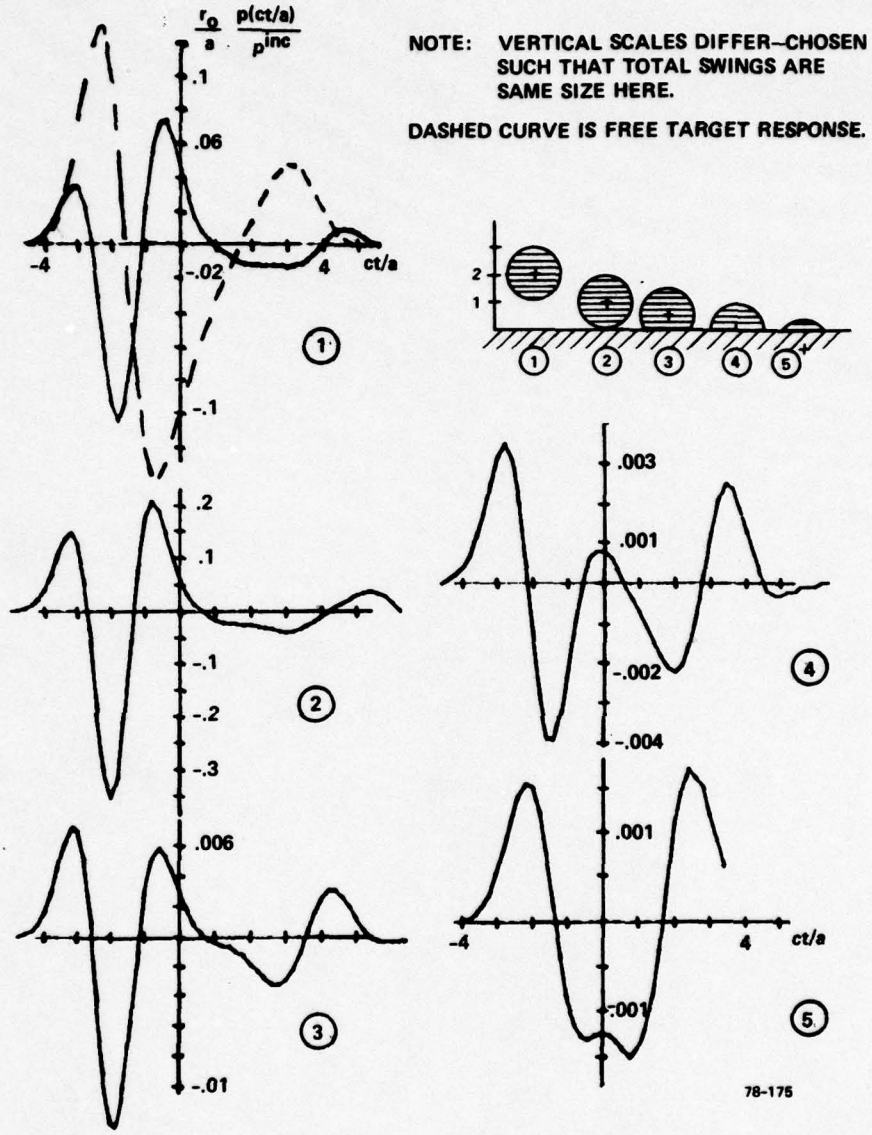

FIG. 17 Smoothed impulse response at various elevations – hard sphere, soft bottom.

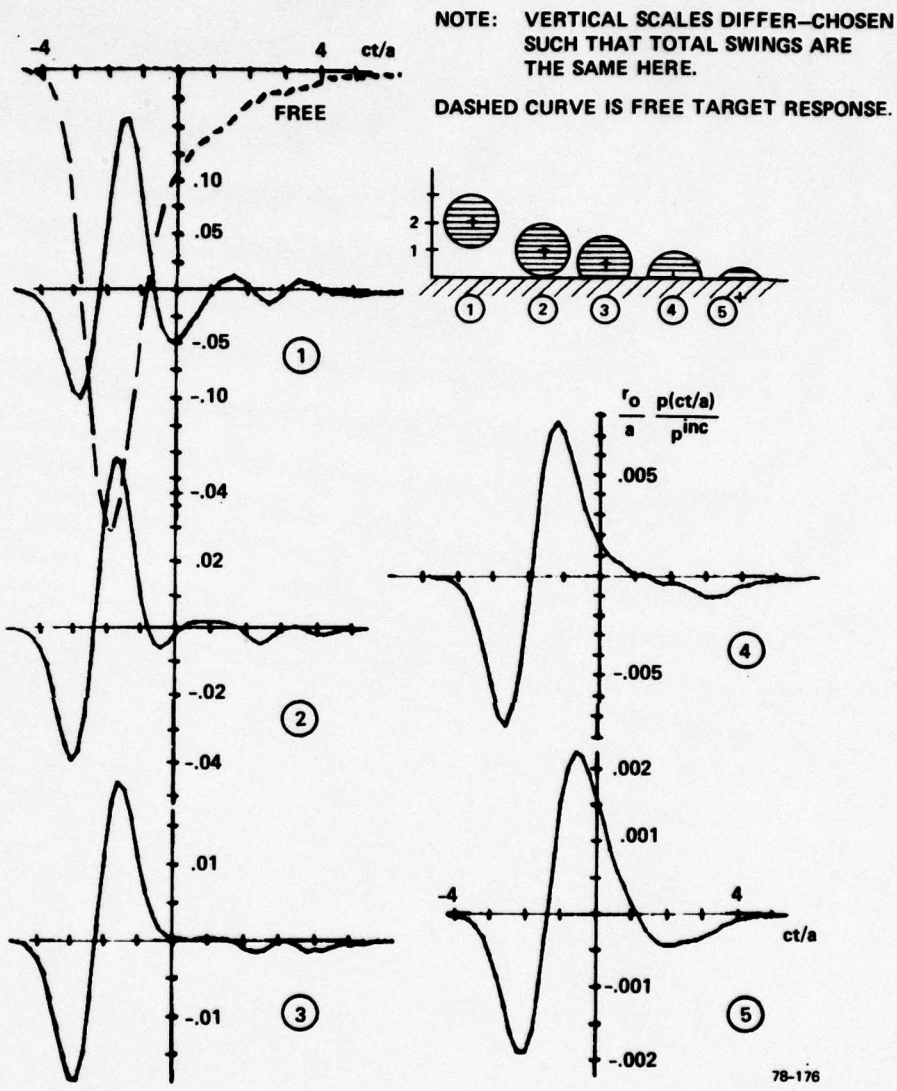

FIG. 18 Smoothed impulse response at various elevations – soft sphere, soft bottom.

the tails. The ratio of the peak amplitudes and their spacing depend strongly on the location of the target. Note that the first three peaks (hard target) or two peaks (soft target) remain at about the same spacing for all elevations of the target. These first peaks must be considered to be the net result of the various specular paths the pressure wave can take (via target, target-bottom, bottom-target, or bottom-target-bottom); whereas the relative timing of the components changes but little in these configurations, that change has a large effect on the amplitude since the components tend to cancel. In the tail of the response we see a signal that increases and moves rapidly to the left as the target is lowered into the bottom. This part of the response is due to a more complicated interaction of bottom and target, involving creepage along the target or bottom.

4.3.2 Upright Cylinder Near a Flat Bottom

In Fig. 19 is shown the response of a hard right-circular cylinder (RCC) near a hard bottom at elevations

(1) $\frac{1}{4}$ of its length above the bottom
(2) On the bottom
(3) $\frac{1}{4}$ penetrating
(4) $\frac{1}{2}$ penetrating, and
(5) 3/4 penetrating.

In Fig. 20 is shown the soft RCC with the same configurations. All the cases are compared with the response from a free target at broadside incidence.

Curve 1 (both hard and soft targets - target above the bottom) shows considerable broadening of the pulse in comparison with the free target response. This can be considered due to the large separation of the target and its image (or due to the large difference in the various paths of specular returns). Associated with the broadening is a reduction in amplitude.

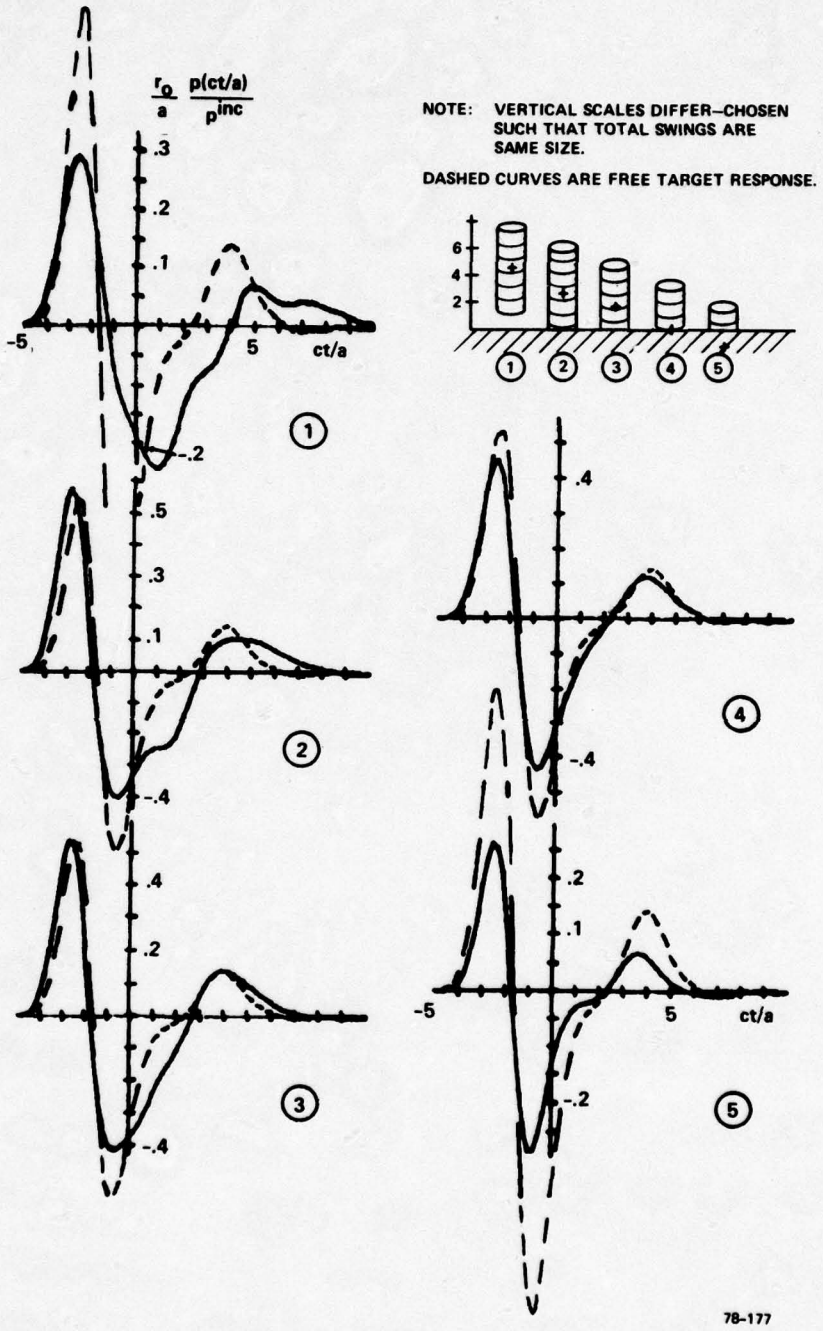

FIG. 19 Smoothed impulse response at various elevations – hard RCC upright (a/L = 1/6), hard bottom.

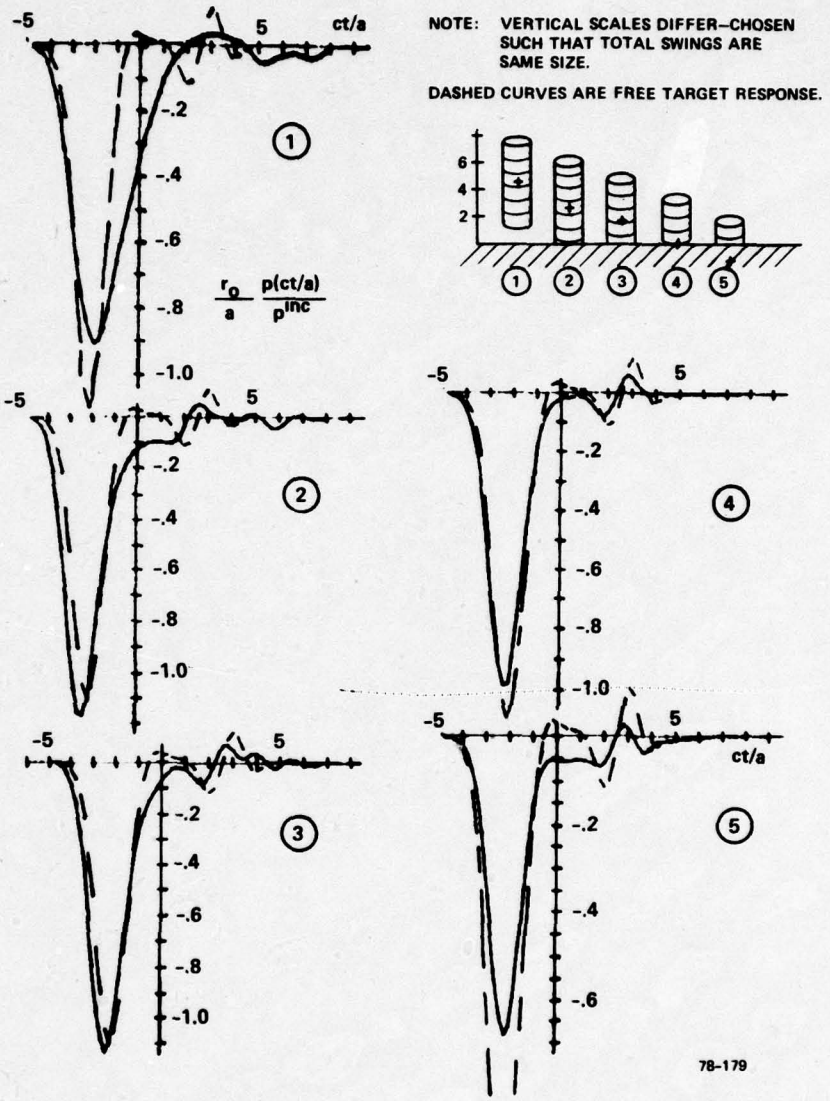

FIG. 20 Smoothed impulse response at various elevations – soft RCC upright (a/L = 1/6), hard bottom.

For the target standing on the bottom (Curve 2), the pulse narrows and increases in amplitude; as the target penetrates the bottom, the response decreases in amplitude (due to the decreased effective size of the target). It should be noted that the comparison made in the figures with the broadside free target response is not the best comparison, since the incidence is different from 90° in all the targets with bottom configurations. Some details of the pulse shapes here are due to the incidence angle: In particular, the broadening or development of the double bump in the negative swing of the hard target response (Fig. 19, Curves 1,2,3) is due to the incidence angle. In summary, we observe that as also observed for the sphere, the presence of a hard bottom has little effect on the pulse shape; the pulse shape being determined primarily by the effective size and orientation of the target with respect to the source. The small doublet wiggles at the ends of the responses in Fig. 20 are thought to be caused by numerical noise in the solution. They become smaller or disappear as either the target patches are made smaller or the pulsewidth is increased.

In contrast to the above observation, a soft bottom causes considerable modification of the return, the shape of the pulse being strongly dependent on the elevation of the target above the bottom. See Figs. 21 and 22 for the hard and soft right-circular cylinders, respectively.

4.3.3 Cylinder on Its Side Near a Flat Bottom

The next configuration evaluated is the right-circular cylinder lying on its side (i.e., with its axis parallel to the bottom). In Fig. 23 are shown the responses for a "free" cylinder and for the cylinder above (center at 1 diameter), on (tangent to), and half-way in the bottom. At the left side of the figure the target is viewed in line with the axis, while the right side of the figure shows the response for broadside inci-

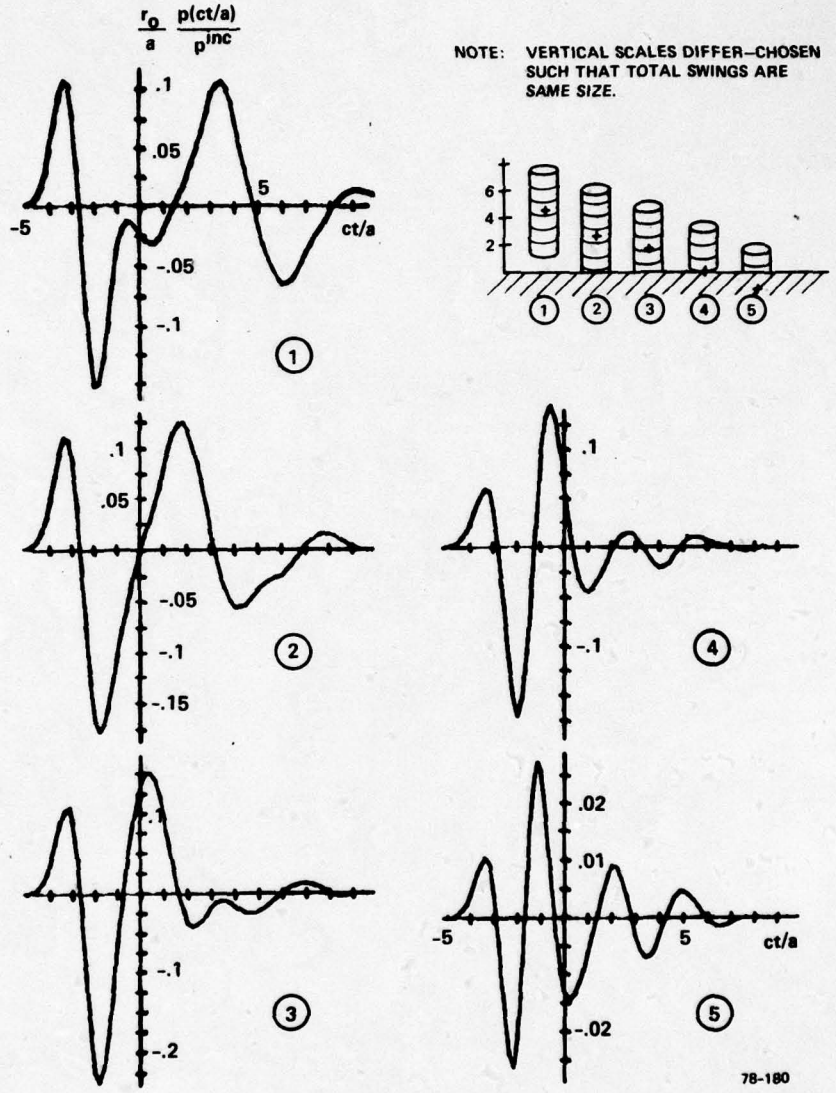

FIG. 21 Smoothed impulse response at various elevations – hard RCC upright (a/L = 1/6), soft bottom.

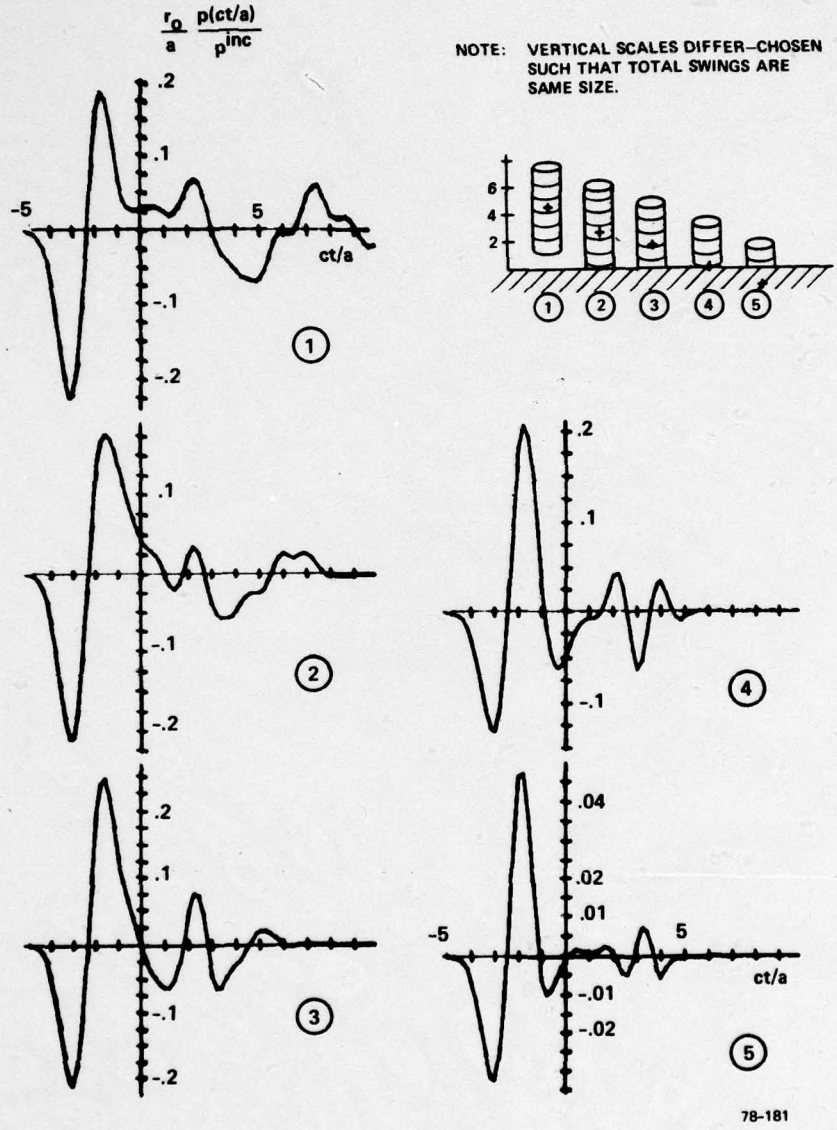

FIG. 22 Smoothed impulse response at various elevations – soft RCC upright (a/L = 1/6), soft bottom.

dence. Again, the point of observation is the same as the source point ($r_o = 10$, $z = 2$). The free target response is shown dashed, superposed on the other plots. The axially viewed response consists of a return from one end followed much later by a response from the far end, while the broadside view response is mainly due to reflection from the cylinder side. We see that the amplitude of the signal increases as the target approaches the bottom, decreasing again as it penetrates the bottom. An interesting effect is the near disappearance of the creep return for the target tangent to the bottom, viewed broadside.

Figure 24 illustrates a soft target with a hard bottom in the same configurations. As in Fig. 20, the wiggles at the ends of the pulses are due to numerical noise in the solution.

Without further comment, we present the target in the same configurations as described above but with a soft bottom in Figs. 25 and 26.

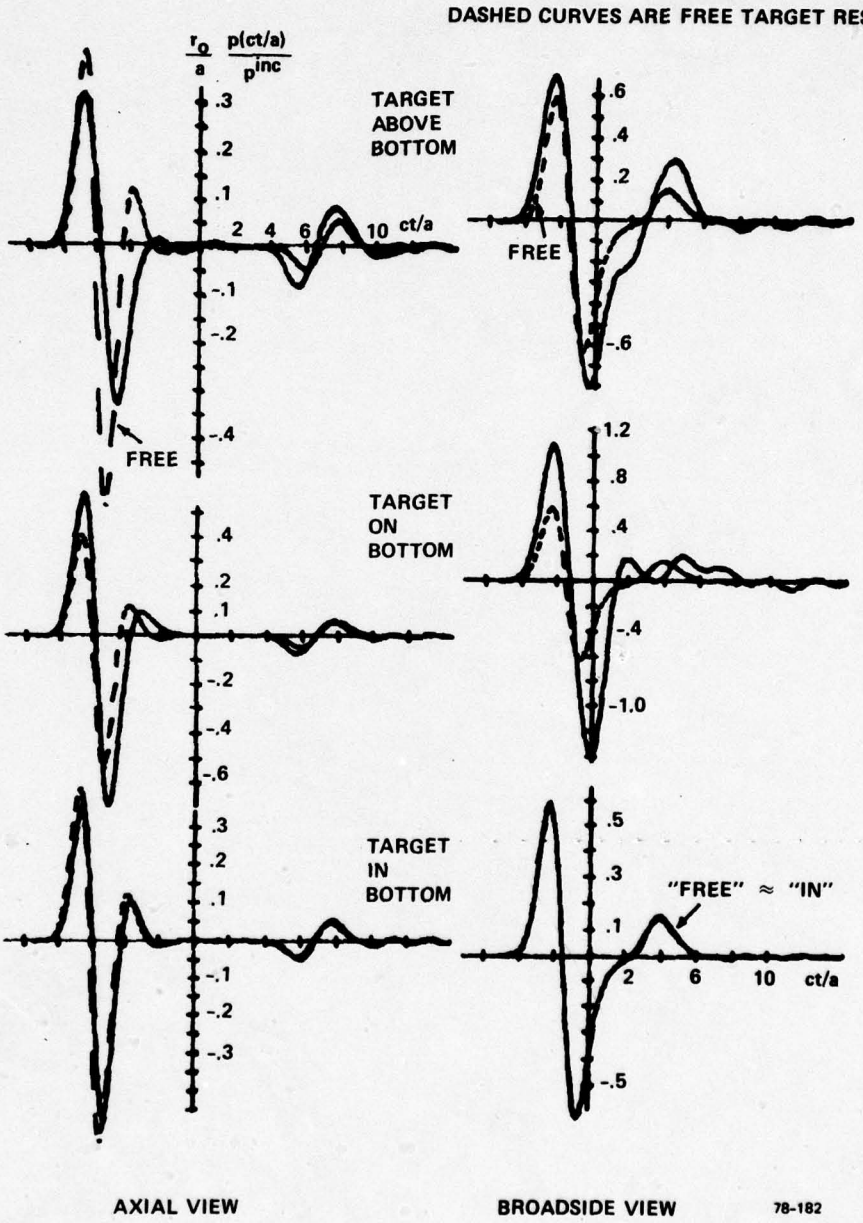

FIG. 23 Smoothed impulse response at two views and three elevations – hard RCC with axis horizontal (a/L = 1/6), hard bottom.

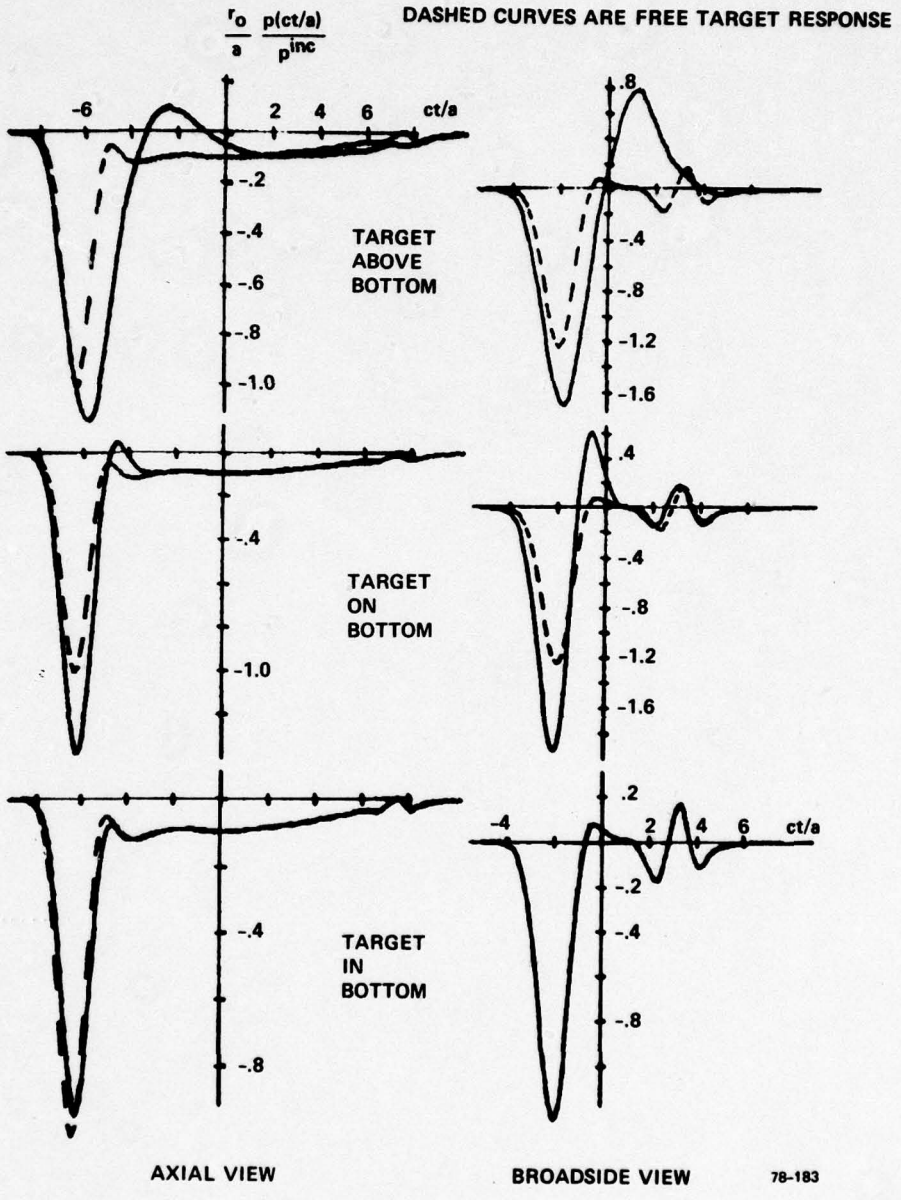

FIG. 24 Smoothed impulse response at two views and three elevations – soft RCC with axis horizontal (a/L = 1/6), hard bottom.

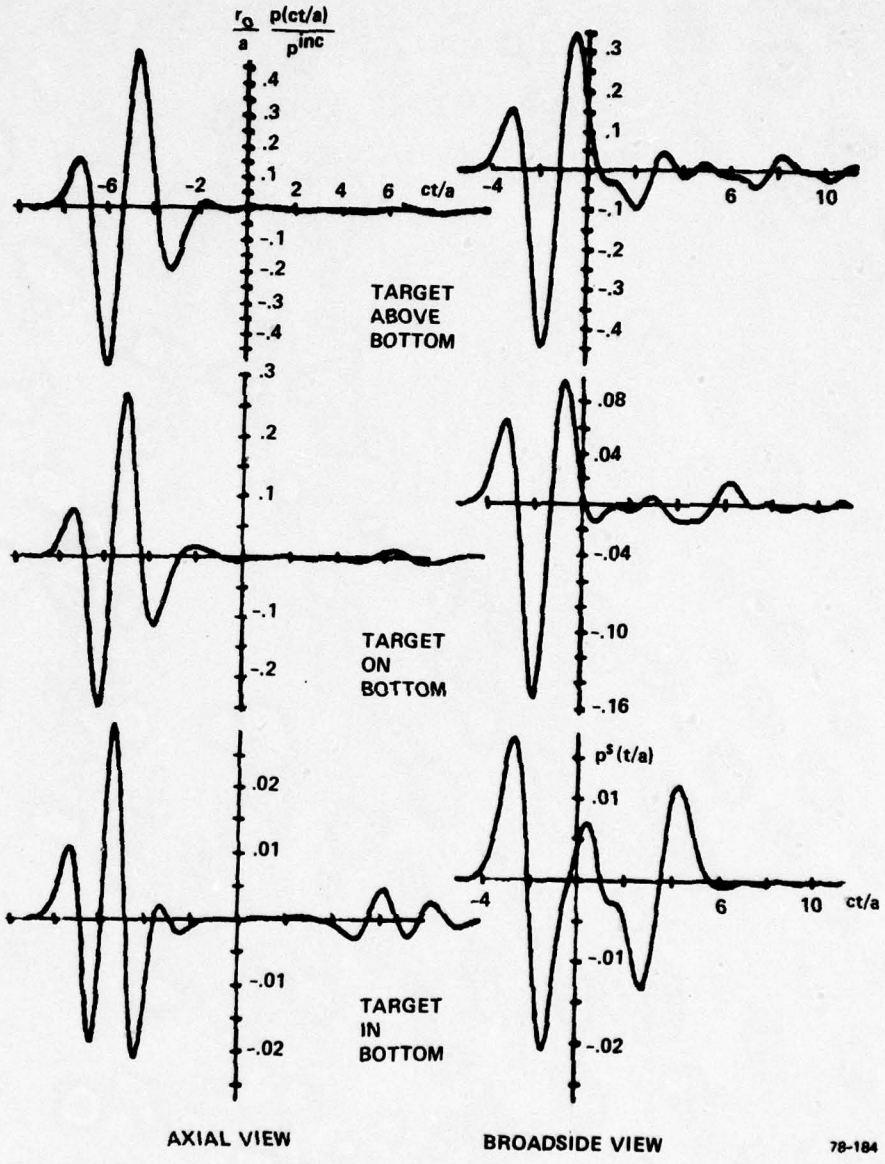

FIG. 25 Smoothed impulse response at two views and three elevations – hard RCC with axis horizontal (a/L = 1/6), soft bottom.

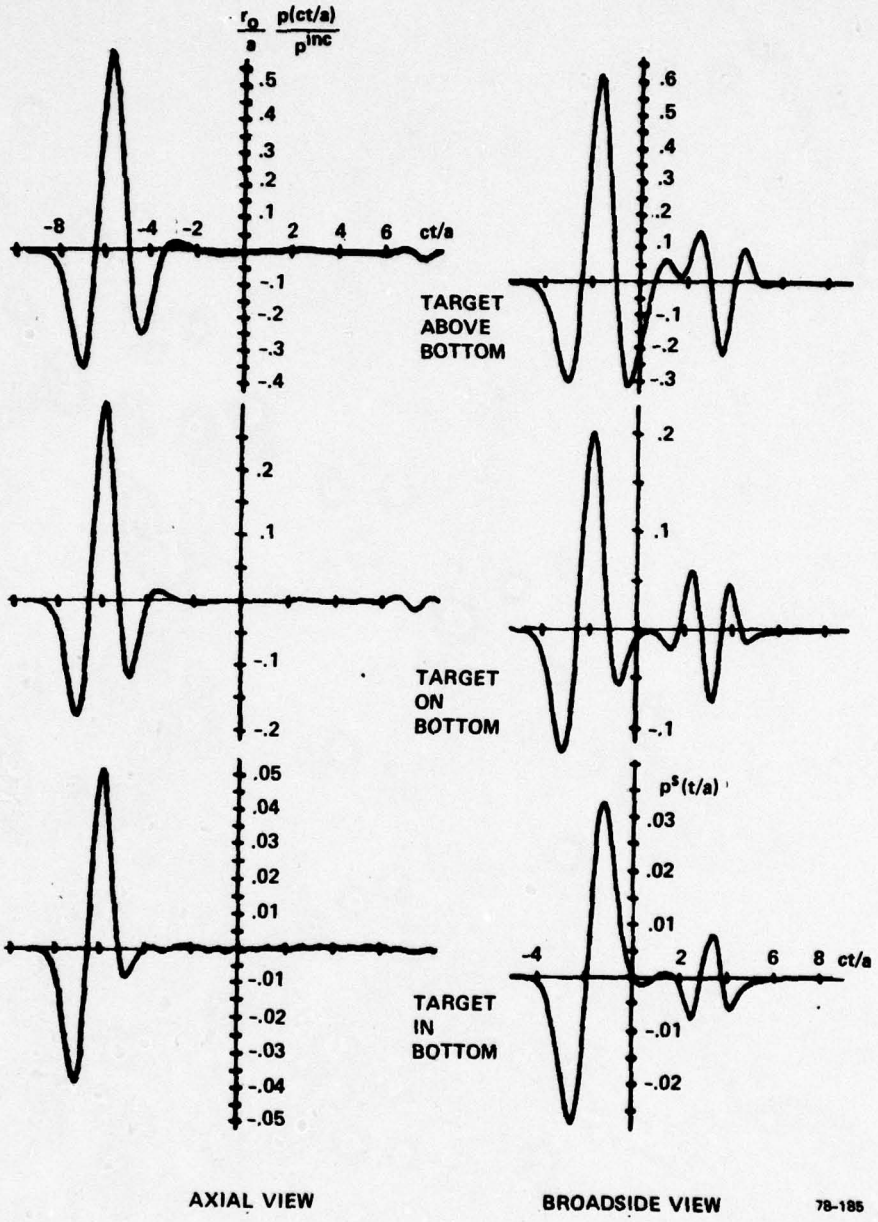

FIG. 26 Smoothed impulse response at two views and three elevations – soft RCC with axis horizontal (a/L = 1/6), soft bottom.

SECTION 5
ANALYSIS OF MEASURED DATA

Measurements were performed by the NCSL on a variety of targets: sphere, right circular cylinder, aluminum, brass, several angles of incidence.

5.1 EXPERIMENTAL PARAMETERS

The description of the experimental arrangement as reported by NCSL [13] is summarized here.

The experimental arrangement is shown in Fig. 27. The input signal was measured at the target location; a reverberation signal without target was measured with the projector and receiver at their normal positions for response measurements. The projector was an EDO Western 6122, the receiver an F-30. The alignment of the target axis for the cylinder was fixed by rotating the target such as to obtain maximum response at axial and normal incidence. Each measurement was repeated 100 times.

The speed of sound in water was determined by signal delay measurement, c_3 = 1491 m/s. The density of salt water was assumed to be 1.026 g/cm^3. The target dimensions were a = 3 cm for the spheres and L/a = 18 cm/3 cm for the cylinders. The materials were Aluminum 6061-T6 and Naval Brass (Alloy 464), for which the elastic parameters are

	Aluminum	Brass	
Y	10	15	10^6 psi
B	10	15.7	10^6 psi
σ	.33	.341	
ρ	2.706	8.394	g/cm^3

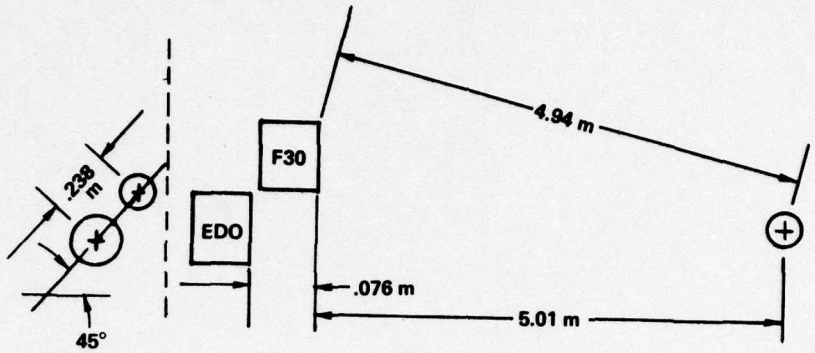

(a)

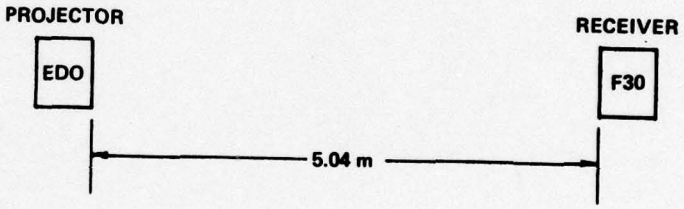

(b)

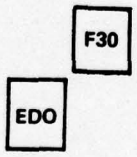

78-186

(c)

FIG. 27 Experimental arrangement: (a) response measurement, (b) input measurement, and (c) reverberation measurement.

The desired parameters c_1 and c_2 were derived from the relations in 2.1.3. For aluminum this gave reasonable results. For brass, the constants on the preceding page were made self-consistent by using $\sigma = 0.341$ rather than the value of .331 quoted in materials handbooks. Anticipating the results of the analysis, it was found that good agreement with measurement was obtained, if c_2 is taken as 2% smaller than from direct use of Y and B in the equations of Section 2.1.3. (It was assumed that this adjustment was justified in the light of the inaccuracy in the preceding parameters.) Accordingly, the parameters used for analysis were

	Aluminum	Brass	Water	
c_1	6108	4400	1490	m/s
c_2	3090	2100		m/s
ρ	2.706	8.394	1.026	g/cm^3

A sample of raw data (aluminum) sphere is given in Fig. 28.

5.2 DATA REDUCTION

The data was put into the standard form discussed in Section 3.8, by scaling time to ct/a, frequency to ka, and the response amplitude by r_o/a. The amplitudes of the response were adjusted by the quoted receiver gain. (Also, for convenience in plotting, the amplitudes of all signals were scaled by an equal factor, F, which disappears when the frequency response is computed.)

The 100 individual pings of the measurements were found to be extremely similar in phase, and in amplitude differed only with a standard deviation of 2% for the responses and 10% for the reverberation. The 100 pings of each measurement were simply averaged, discarding only those (few) pings which showed spurious behavior.

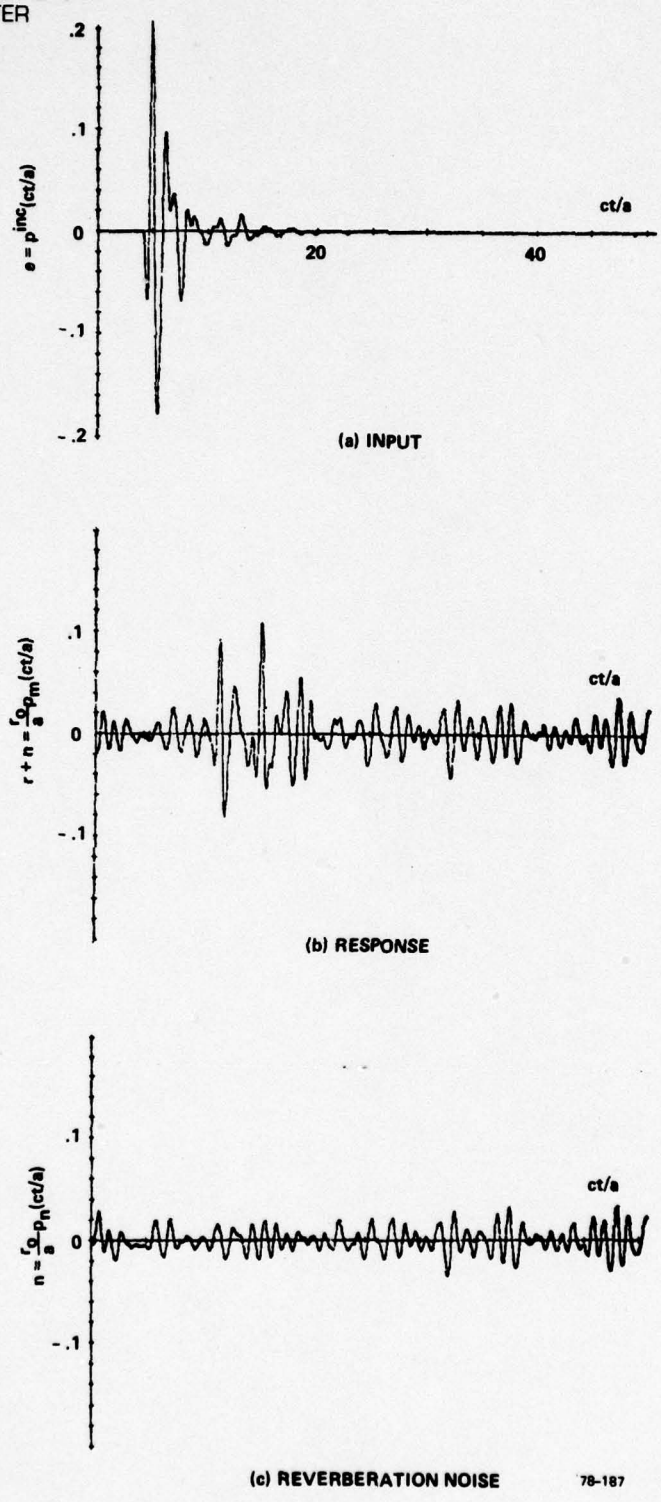

FIG. 28 Typical response, input, reverberation in time domain (brass sphere 0°).

Figure 28 illustrates an example of scaled but unprocessed measurements (for the brass sphere at 0°). The incident pressure is taken as the voltage at the receiver, v_e, (since the receiver was placed at the target position for this measurement), scaled by the receiver gain, G_e, and an arbitrary factor, F. That is:

$$e(ct/a) = p^{inc}(ct/a) = F \cdot 10^{-(G_e/20)} v_e(ct/a).$$

The measured response, which consists of the actual response, r, plus noise, n, is scaled similarly and also by the factor r_o/a. That is:

$$r + n(ct/a) = \frac{r_o}{a} \cdot F \cdot 10^{-(G_m/20)} v_m(ct/a).$$

The scaled reverberation noise signal is represented as

$$n(ct/a) = \frac{r_o}{a} \cdot F \cdot 10^{-(G_n/20)} v_n(ct/a).$$

These same signals, transformed to the frequency domain, are illustrated in Fig. 29.

The scaled response with noise subtracted is then

$$r(ct/a) = \frac{r_o}{a} \cdot F \cdot \left(10^{-(G_m/20)} v_m(ct/a) - 10^{-(G_n/20)} v_n(ct/a) \right).$$

It was expected that direct subtraction of the reverberation signal would yield a clean response signal. This was not the case. Some reverberation noise remained in the precurser and after signal end. The result of noise subtraction is shown in the first curve of Fig. 30. (Arbitrary adjustment of reverberation amplitude did not affect the overall result.) A possible cause of this problem is environmental changes.

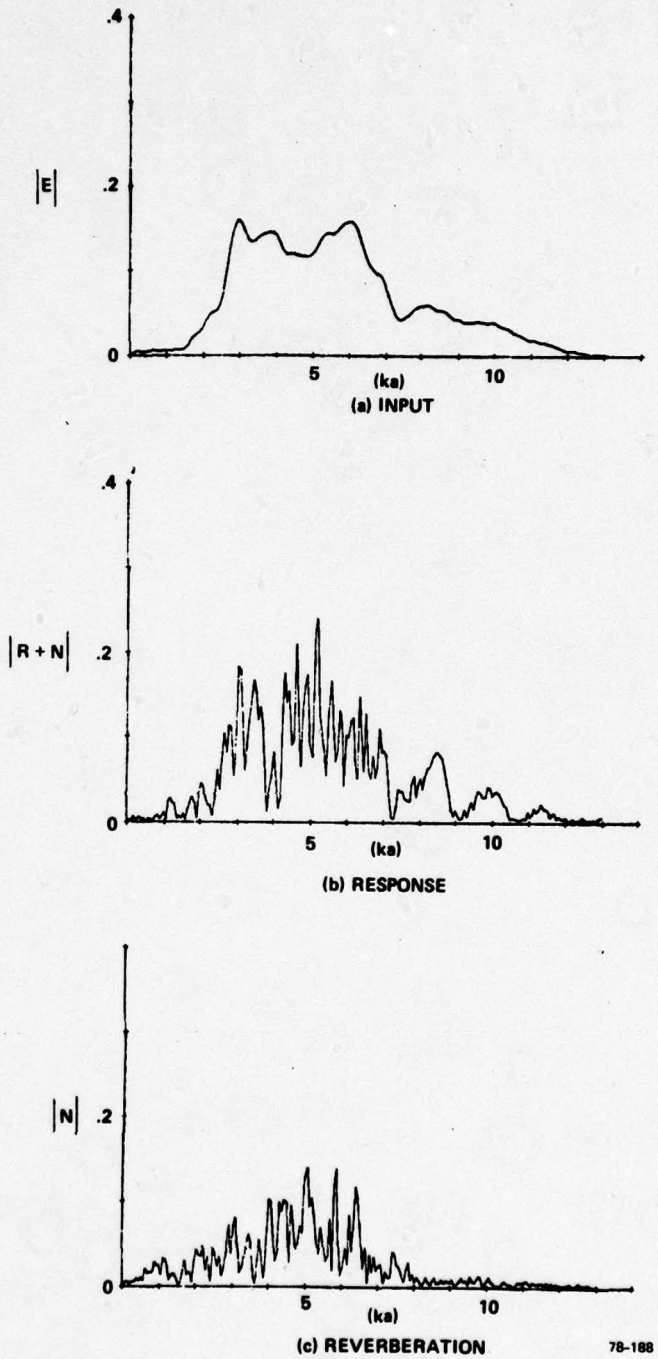

FIG. 29 Typical response, input, reverberation in frequency domain (brass sphere 0°).

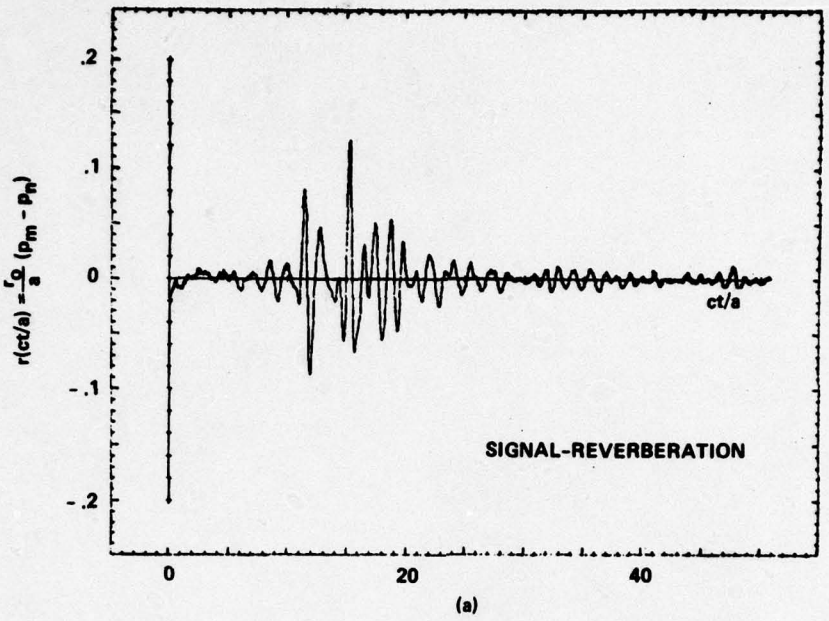

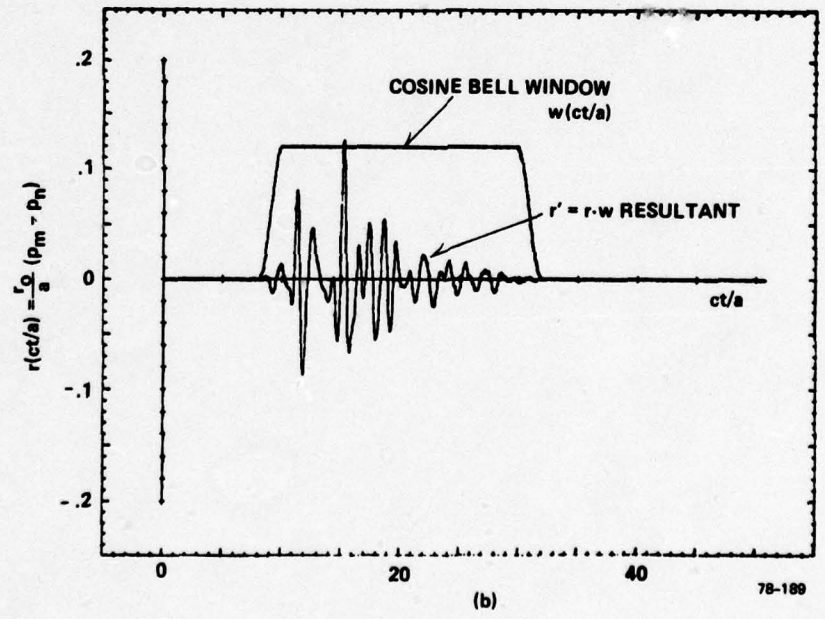

FIG. 30 Signal processing (brass sphere 0°).

The effect of the remaining noise is to introduce spikyness in the frequency response. To reduce this effect, smoothing was introduced by the application of a cosine bell window, w, to the signal, which eliminated the initial and final reverberation. Fig. 30(b) shows the signal after reverberation subtraction and application of the window, and also shows the window used. Figure 31 illustrates these results of signal processing in the frequency domain. The (complex) frequency response of the target was then found: $H(ka) = [R(ka) * W(ka)]/E(ka)$. The result of this process is shown in Fig. 32 for the aluminum sphere and in Fig. 33 for the naval brass sphere. The results are shown for the two aspects (0° and 45°) at which the spheres were measured. The plotted quantity is the magnitude of H(ka). Note that the input signal occupied a band of $ka = 1.5$ to 12, so that H(ka) outside these limits has no meaning.

5.3 COMPARISON WITH CALCULATIONS

5.3.1 Spheres

A slight directionality can be observed in comparing the 0° and 45° aspects, indicating either a slight anisotropy of the material, or an error due to changes in the reverberation. The latter is likely, since the reverberation spectrum was greatest at those frequencies where the differences are observed.

Figures 32 and 33 also show the theoretical responses superposed as dotted curves. The results are in close agreement with respect to both amplitude and alignment of the major nulls. (The value of c_2 for brass was adjusted by 2% as noted in Section 5.1.) The faster small wiggles with null spacing at $\delta(ka) = 1.22$ does not agree as well, but is clearly present in the response. The small and deep wiggles can thus be used to estimate the size and composition of the target, independently of size determination based on response amplitude. This is perhaps even more apparent if the signals are observed in the time domain (see Section 4.1)

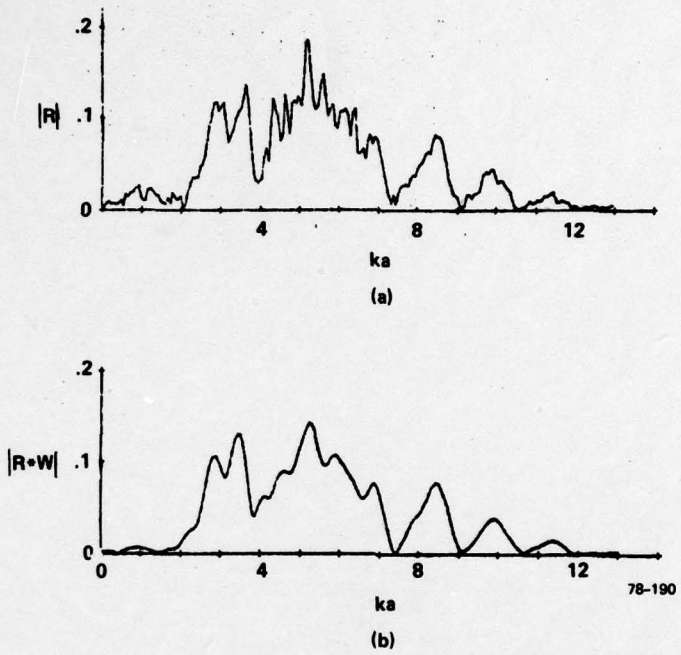

FIG. 31 Signal processing – frequency domain: (a) signal after reverberation noise subtraction; and (b) result of (a).

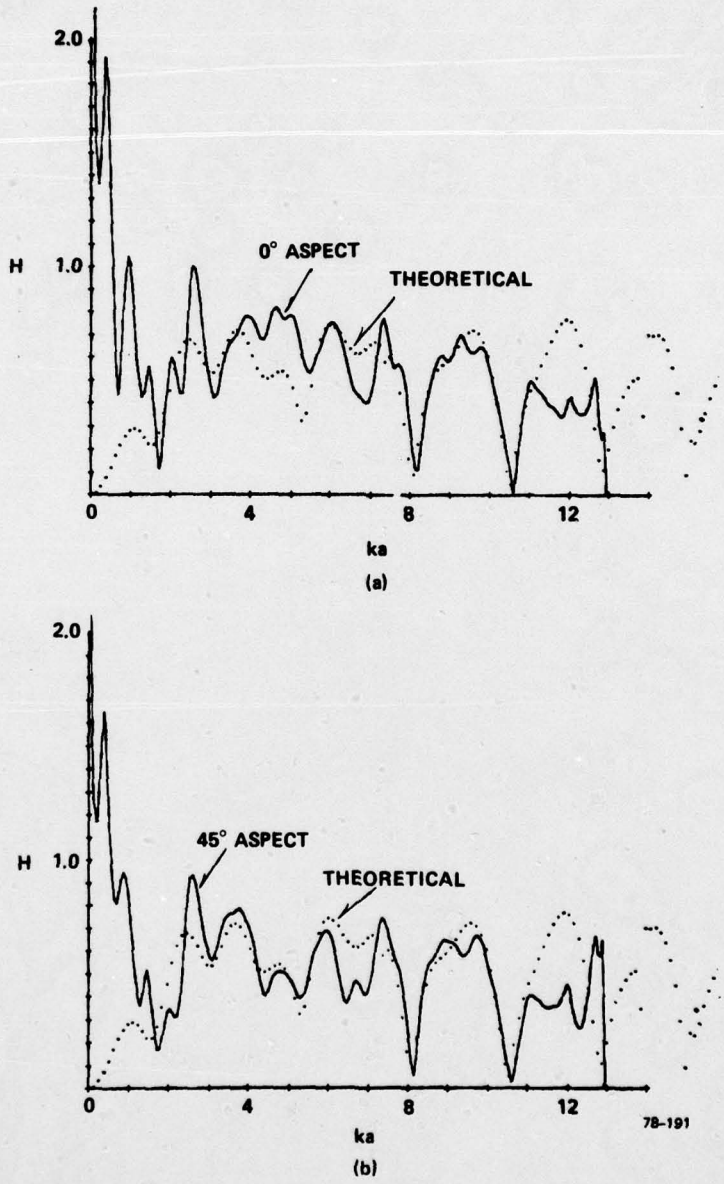

FIG. 32 Measured and theoretical response of sphere (aluminum).

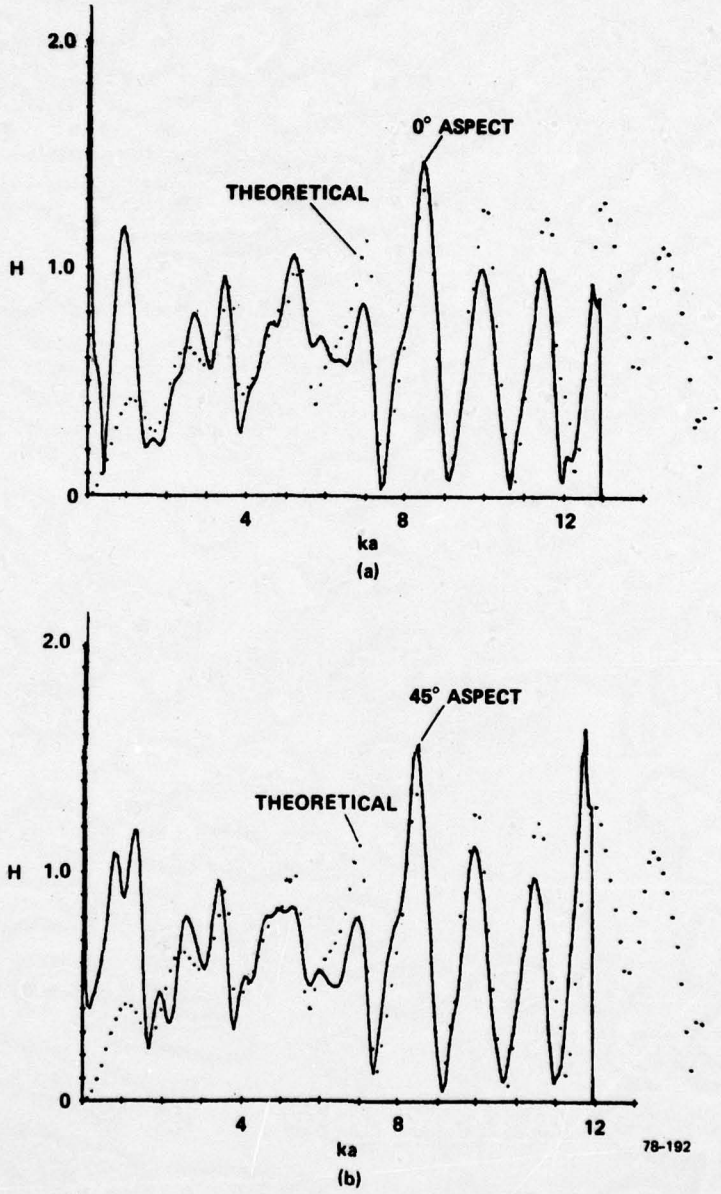

FIG. 33 Measured and theoretical response of sphere (brass).

which yields directly circumferential size from the creep return and target material from the wiggle in the response near t = 0. Figure 34 illustrates the theoretical responses in the time domain for the two spheres calculated by convolving the input, e, with the theoretical H(ka):

$$r'(ct/a) = F^{-1}\Big(F\big(e(ct/a)\big) \cdot H(ka)\Big) .$$

The agreement with measurements is seen to be close, differing somewhat in amplitude, but not in zero crossings.

5.3.2 Cylinders

The frequency responses of the cylinders at 0° and 90° are shown in Figures 35 and 36 for aluminum and brass respectively. Superposed on these signals is the high frequency asymptotic response. For 0° (end-on) aspect the latter is given by

$$H(ka) = 0.5\ (ka)$$

for 90° (broadside) aspect by

$$H(ka) = \frac{0.5}{\sqrt{\pi}}\ \frac{L}{a}\ (ka)^{1/2} .$$

It can be seen that the high frequency approximation is not a good model for the elastic cylinders in this frequency range.

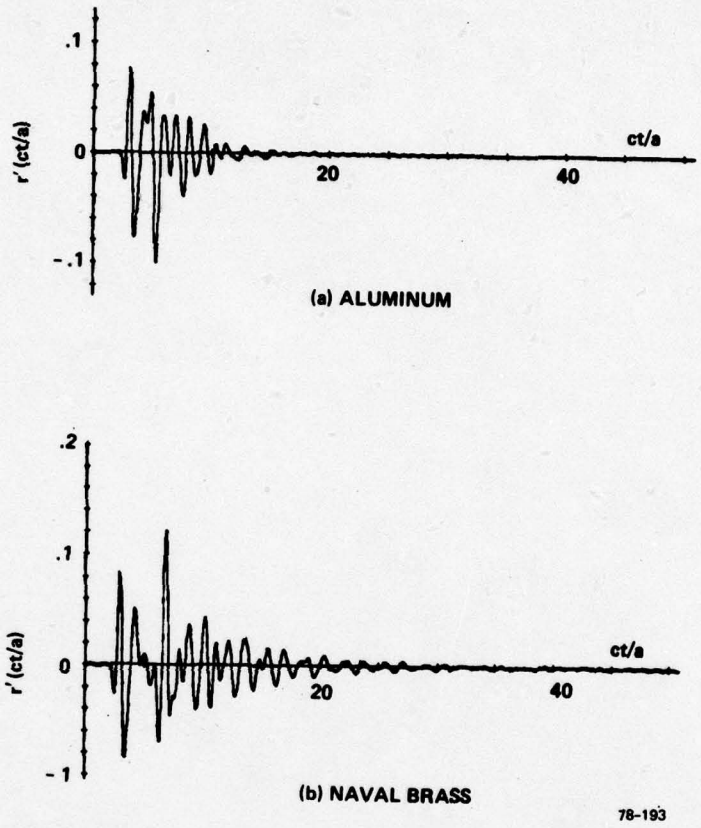

FIG. 34 Theoretical response of sphere with experimental input signal.

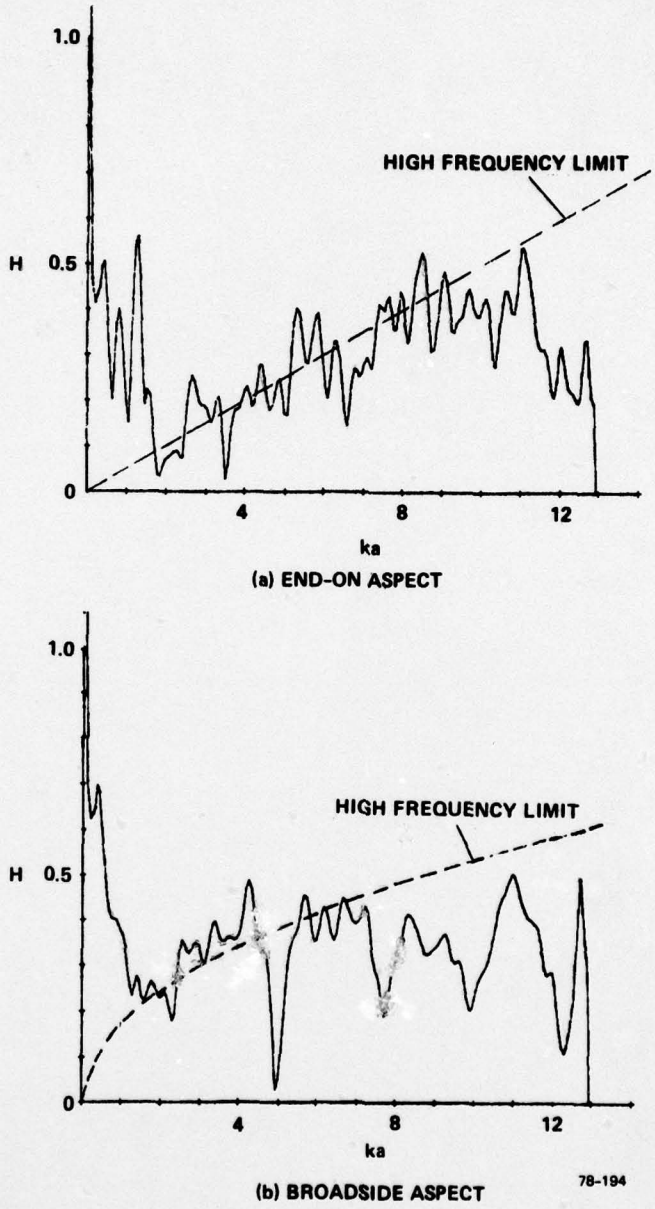

FIG. 35 Measured response of cylinder (aluminum).

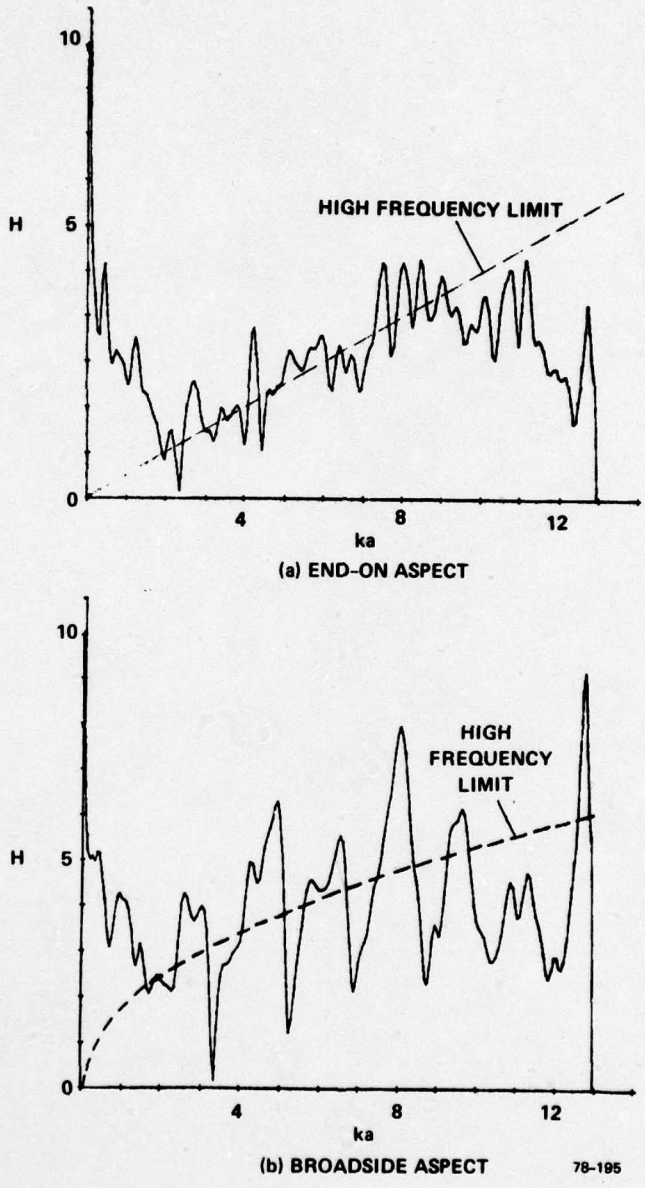

FIG. 36 Measured response of cylinder (brass).

SECTION 6
FORMULATION FOR HULLED BODIES

We consider now the problem of a fluid-filled elastic shell, submerged in a fluid. Following the formulation of Section 2 and writing $\bar{u}_1$ for the interior fluid, $\bar{u}_2$ for the shell, and $\bar{u}_3$ for the exterior fluid, we thus have the wave equations:

$$\frac{\partial^2}{\partial t^2}(\nabla \cdot \bar{u}_1) = c_1^2 \nabla^2(\nabla \cdot \bar{u}_1) \tag{54}$$

$$\frac{\partial}{\partial t^2}(\nabla \cdot \bar{u}_3) = c_3^2 \nabla^2(\nabla \cdot \bar{u}_3) \tag{55}$$

in the fluids, and

$$\frac{\partial^2}{\partial t^2}(\nabla \cdot \bar{u}_2) = c_{21}^2 \nabla^2(\nabla \cdot \bar{u}_2) \tag{56}$$

$$\frac{\partial^2}{\partial t^2}(\nabla \times \bar{u}_2) = c_{22}^2 \nabla^2(\nabla \times \bar{u}_2) \tag{57}$$

in the solid shell, where c_{21} and c_{22} are the shell compressional and shear velocities respectively.

These equations can be solved in the fashion presented in Section 2.2.2 by writing the space-time integral equations for the boundary points. The result is an integral equation for $(\nabla \cdot \bar{u}_1)$ integrated over the interior boundary, an integral equation for $(\nabla \cdot \bar{u}_3)$ integrated over the exterior boundary, and integral equations for $(\nabla \cdot \bar{u}_2)$ and $(\nabla \times \bar{u}_2)$ integrated over the sum of the interior and exterior boundaries. These STIE's are then solved simultaneously by using the boundary conditions of Section 2.1.4: one set of boundary conditions for each surface.

Such a "full-scale" solution thus requires the evaluation of 4 integral equations, the use of boundary relations on both interior and exterior shell surfaces, and the storage of 11 field variables (2 more than for the case of the elastic solid in a fluid). The solution process is thus a straightforward extension of the solution for the elastic solid problem.

Alternatively, the problem can be considerably simplified if the shell can be treated as a thin membrane. By "thin" is meant that there is no variation in $\bar{u}$ in the normal direction (i.e., across the membrane) and that the only stresses in the shell are tangential or surface tensions. The first boundary condition (see Section 2.1.4) then becomes

$$u_{n_1} = u_{n_2} = u_{n_3} \quad \text{(continuity of normal displacement).} \tag{58}$$

The second boundary condition (continuity of normal stress) holds independently on the interior and exterior surface of the membrane, but not necessarily from interior fluid to exterior fluid, as the thickness of the membrane is reduced to zero. The membrane permits a discontinuity of normal stress (i.e., pressure) to exist between the fluids.

The forced wave equation for the normal displacement of a thin membrane is [8]

$$(\rho_2 d) \frac{\partial^2 u_n}{\partial t^2} - T \nabla_s^2 u_n = p_1 - p_3 \tag{59}$$

Here,

d is the thickness of the membrane,

$(\rho_2 d)$ is the density/unit area,

T is the surface tension (force/unit length),

∇_s^2 is the surface Laplacian,

$p_1 - p_3$ is the discontinuity in excess pressure,

$\hat{n}$ is directed into medium 3 (or outward).

The surface tension, T, is in general a function of the surface coordinates. For a membrane that is free to move in the fluid, T is proportional to the difference in ambient pressures between media 1 and 3 and to the equilibrium surface curvature.

Writing our equations in terms of excess pressure p, rather than $(\nabla \cdot \bar{u})$ (see Section 2.1.5), we can thus summarize:

Wave equations:

$$\ddot{p}_1 = c_1^2 \nabla^2 p_1 , \tag{60}$$

$$\ddot{p}_3 = c_3^2 \nabla^2 p_3 , \tag{61}$$

which have the STIE solutions on the boundary (see Section 2.3.1):

$$p_1(\bar{r},t) = \frac{1}{2\pi} \int_S \left\{ \frac{1}{R} \frac{\partial p_1'}{\partial n'} - (\hat{n}' \cdot \hat{R}) \, L_1 \, p_1' \right\} dS' , \tag{62}$$

$$p_3(r,t) = 2p^{inc} - \frac{1}{2\pi} \int_S \left\{ \frac{1}{R} \frac{\partial p_3'}{\partial n'} - (\hat{n}' \cdot \hat{R}) \, L_3 \, p_3' \right\} dS' . \tag{63}$$

These are solved simultaneously, using the condition (59) and the relations (see Section 2.1.5)

$$\left.\begin{aligned} \frac{\partial p_1}{\partial n} &= -\rho_1 \ddot{u}_n \\ \frac{\partial p_3}{\partial n} &= -\rho_3 \ddot{u}_n \end{aligned}\right\} \qquad (64)$$

We see that the solution also requires the formation of $\nabla_s^2 u_n$ on the surface and the integration of $\ddot{u}_n$ in time to give u_n.

SECTION 7
SUMMARY

In this report we have formulated in detail the general solution to time domain acoustic scattering from elastic targets, both solid and thin-shelled. The formulation was implemented for solids with rotational symmetry at arbitrary angle of incidence. The results for the hard, soft, and fluid approximations were very good for both smooth (spherical) bodies and bodies with edges (right circular cylinder). The full elastic solution still suffers from numerical instabilities believed to be caused by inaccuracies in the formation of surface derivatives. Also, it is believed that special treatment is required at sharp edges for the full elastic case.

The responses of spheres and right circular cylinders on or near a bottom were calculated for the cases of hard and soft targets and bottoms. A method of images was employed.

The responses of elastic spheres were calculated according to the classical solution. Using this solution, the effect of elastic parameters on the response was analyzed.

The results of measurements taken at NCSL were compared with calculations. It was found that the hard, fluid, elastic target models, in that order, result in increasingly good approximations to the measured responses for incident waves in the resonance region.

SPERRY RESEARCH CENTER

SECTION 8

REFERENCES

1. J.J. Faran, "Sound Scattering by Solid Cylinders and Spheres," J.A.S.A. 23-4, July 1951.

2. R. Hickling, "Analysis of Echoes from a Solid Elastic Sphere in Water," J.A.S.A. 34-10, October 1962.

3. L. Knopoff, "Diffractior of Elastic Waves," J.A.S.A. 28-2, March 1956.

4. M.B. Friedman, R. Shaw, "Diffraction of Pulses by Cylindrical Obstacles of Arbitrary Cross-Section," Trans. ASME, March 1962.

5. C.L. Bennett, "A Technique for Computing Approximate Electromagnetic Impulse Response of Conducting Bodies," Ph.D. Dissertation, Purdue University, Lafayette, Indiana, August 1968.

6. C.L. Bennett, "The Numerical Solution of Transient Electromagnetic Scattering Problems," SCRC-RP-77-55, August 1977.

7. E.M. Kennaugh and R.L. Cosgriff, "The Use of Impulse Response in Electromagnetic Scattering Problems," 1958 IRE Nation Convention Record, Part I, pp. 72-77.

8. R.B. Lindsay, "Mechanical Radiation," McGraw-Hill, 1960.

9. C.L. Bennett and R.M. Hieronymus, "Solution of Acoustic Space-Time Integral Equations for Soft and Hard Boundary Conditions," SCRC-RR-74-29, November 1974.

10. H. Mieras, C.L. Bennett, "Solution of Acoustic Space-Time Integral Equations for Hard or Soft Targets in the Presence of Hard or Soft Planes," SCRC-RR-76-4, February 1976.

11. H. Mieras and C.L. Bennett, "Bionic Sonar Target Response Predictions," SCRC-RR-76-39, July 1976.

12. V.C. Anderson, "Sound Scattering from a Fluid Sphere," J.A.S.A. 22-4, July 1950.

13. D.P. Skinner, J. Nelander, NCSL, Panama City, Florida, unpublished communication, March 1978.

APPENDIX A

REFORMULATION OF THE SPACE-TIME INTEGRAL EQUATIONS, USING INTEGRATION BY PARTS

An alternate approach to solving the STIE's using integration by parts is described. This method requires the storage of only 4 or 5 surface variables (rather than 9), at the expense of greater complexity. Instability difficulties led to abandonment of this method in favor of the less complex approach in the body of the report.

We start here with equations (24)-(26) and divide the integral into a self and non-self part. For equation (24) we had obtained

$$(1-\varepsilon)(\nabla\cdot\bar{u}_3) + \gamma\frac{\partial^2 u_n}{c_3^2\partial t^2} = 2(\nabla\cdot\bar{u}_3)^{inc} - \frac{1}{2\pi}\int_{NS}\left\{\frac{1}{Rc_3^2}\frac{\partial^2 u_n'}{\partial t^2} - (\hat{R}\cdot\hat{n}')\,L_3(\nabla\cdot u_3')\right\}dS'. \tag{A-1}$$

We plan to store the quantities appearing under the integral u_n, $\nabla\cdot\bar{u}_3$. For equation (25), we proceed similarly, using

$$\frac{\partial}{\partial n}(\nabla\cdot\bar{u}) = \frac{1}{c_1^2}\frac{\partial^2 u_n}{\partial t^2} - \frac{2c_2^2}{c_1^2}\nabla_s^2 u_n \tag{A-2}$$

(derived from B.C. 4 of Section 2), and using B.C. 2 to eliminate $\nabla\cdot\bar{u}$ from the equation. We then obtain for the self-integral:

$$I_{s1} = \frac{1}{2\pi}\int_{self}\left\{\frac{1}{Rc_1^2}\frac{\partial^2 u_n'}{\partial t^2} - (\hat{R}\cdot\hat{n}')\left(\frac{\rho_3 c_3^2}{\rho_1 c_1^2}\right)L_1(\nabla\cdot\bar{u}_3')\right.$$

$$\left. - (\hat{R}\cdot\hat{n}')\left(\frac{2c_2^2}{c_1^2}\right)L_1(\nabla_s\cdot\bar{u}') - \frac{2c_2^2}{Rc_1^2}\nabla_s^2 u_n'\right\}dS' \tag{A-3}$$

AD-A081 710 SPERRY RESEARCH CENTER SUDBURY MASS F/G 20/1
ACTIVE SONAR MODELING.(U)
AUG 78 H MIERAS, C L BENNETT N61339-77-C-0105
UNCLASSIFIED SCRC-CR-78-44 NL

2 OF 2
AD A081710

END
DATE FILMED
4-80
DTIC

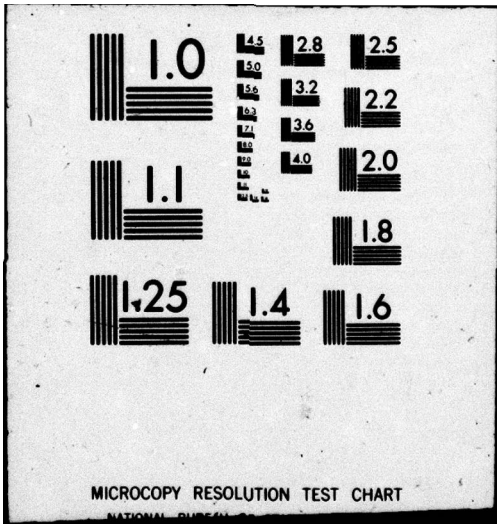
1.0
1.1
1.25
1.4
1.6
1.8
2.0
2.2
2.5
2.8
3.2
3.6
4.0
4.5
5.0
5.6
6.3
MICROCOPY RESOLUTION TEST CHART

$$I_{s1} = \gamma \frac{\partial^2 u_n}{c_1^2 \partial t^2} - \varepsilon\left(\frac{\rho_3 c_3^2}{\rho_1 c_1^2}\right)(\nabla \cdot \bar{u}_3) - \gamma\left(\frac{2\, c_2^2}{c_1^2}\right)\nabla_s^2\, u_n - \varepsilon\left(\frac{2\, c_2^2}{c_1^2}\right)(\nabla_s \cdot \bar{u}) \quad . \qquad \text{(A-4)}$$

The non-self integral (which has the same argument as in equation (A-3)), contains in addition to u_n and $\nabla \cdot \bar{u}_3$, the surface derivatives of $\bar{u}$. We wish to eliminate these, using integration by parts, which will transform the surface derivatives into time derivatives. We use the integration by parts formula for an open surface:

$$\int_S \phi\, (\nabla_s \cdot \bar{A})\, dS = - \oint_C \hat{n}_c \cdot \phi \bar{A}\, d\ell - \int_S \bar{A} \cdot \nabla\phi\, dS \qquad \text{(A-5)}$$

Here, C is the contour bounding the surface, S, of integration and $\hat{n}_c$ lies in S, normal to C pointing into S (i.e., pointing out of self-patch). For example, identifying $\bar{A}$ as $\bar{u}_s$, ϕ as $(\hat{R} \cdot \hat{n}')L_1$ (where the subscript S denotes surface components), the term in the non-self integral:

$$T = - \frac{1}{2\pi} \int_{NS} (\hat{R} \cdot \hat{n}') \left(\frac{2\, c_2^2}{c_1^2}\right) L_1 (\nabla_s \cdot \bar{u}')\, dS'$$

becomes

$$T = \frac{1}{2\pi}\left(\frac{2\, c_2^2}{c_1^2}\right) \oint_{c_s} (\hat{R} \cdot \hat{n}')\; L_1 (\hat{n}_c \cdot \bar{u}_s')\, d\ell' + \frac{1}{2\pi}\left(\frac{2\, c_2^2}{c_1^2}\right) \int_{NS} (\hat{R} \cdot \hat{n}')\; O_1 (\hat{R} \cdot \bar{u}_s')\, dS' \qquad \text{(A-6)}$$

where

O_1 is the operator $\left(\frac{3}{R^3} + \frac{3}{Rc_1^2}\frac{\partial}{\partial \tau} + \frac{1}{Rc_1^2}\frac{\partial^2}{\partial \tau^2}\right)$. (A-7)

This is obtained from the identity

$$\nabla'\phi \equiv \nabla'(\hat{R}\cdot\hat{n}')\,L_1 = (\hat{R}\cdot\hat{n}')\;\hat{R}\;O_1 - \frac{\hat{n}'}{R}\,L_1 \quad . \tag{A-8}$$

The contour integral about the self-patch can be evaluated, using a Taylor series expansion, and results in terms similar to those in equation (A-4), and additional terms involving the difference in principal curvatures.

Similarly, the non-self integral of $\int_{NS} \nabla_s^2 u_n'\, dS'$ can be evaluated by applying the integration by parts formula twice. The final result for the transformed $\nabla\cdot\bar{u}$ equation is

$$\left[(1+\varepsilon)\left(\frac{\rho_3 c_3^2}{\rho_1 c_1^2}\right)\right](\nabla\cdot\bar{u}_3) - \left[\gamma\left(1-\frac{c_2^2}{c_1^2}\right)\right]\frac{\partial^2 u_n}{c_1^2\partial t^2} =$$

$$\tilde{I}_{s1} + \frac{1}{2\pi}\int_{NS}\left\{\frac{1}{R}\left(1-\frac{2c_2^2}{c_1^2}\right)\frac{\partial^2 u_n'}{c_1^2\partial t^2} - (\hat{R}\cdot\hat{n}')\left(\frac{\rho_3 c_3^2}{\rho_1 c_1^2}\right)L_1(\nabla\cdot\bar{u}_3')\right.$$

$$\left. + \left(\frac{2c_2^2}{c_1^2}\right)(\hat{R}\cdot\hat{n}')\;O_1(\hat{R}\cdot\bar{u}_s')\right\} dS' \tag{A-9}$$

where

$$\tilde{I}_{s1} = -\left(1+\frac{\varepsilon}{2}\right)\left(\frac{2c_2^2}{c_1^2}\right)(\nabla_s\cdot\bar{u}) - \frac{\gamma}{4}\left(\frac{2c_2^2}{c_1^2}\right)\nabla_s^2 u_n + \left(\frac{2c_2^2}{c_1^2}\right)\frac{u_n}{\gamma}$$

$$+ \frac{\gamma}{2}\left(\frac{2c_2^2}{c_1^2}\right)\left(\frac{K_1-K_2}{4}\right)\left(\frac{\partial u_x}{\partial x} - \frac{\partial u_y}{\partial y}\right)$$

Only the quantities $\bar{u}$ and $(\nabla \cdot \bar{u}_3)$ appear under the integral sign, which (four) quantities need to be stored. The terms in $\tilde{I}_{s1}$ need to be evaluated by numerical surface differentiation of $\bar{u}$. Equations (A-9) and (A-1) can then be solved simultaneously for $(\nabla \cdot \bar{u}_3)$ and $\partial^2 u_n/\partial t^2$. Furthermore, using the representation

$$\frac{\partial^2 u_n}{\partial t^2}(t) = \frac{u_n(t + \Delta t) - 2\, u_n(t) + u_n(t - \Delta t)}{(\Delta t)^2} \qquad \text{(A-10)}$$

$u_n(t)$ can be evaluated for the next time point.

In a similar manner, the $(\nabla \times \bar{u})$ equation can be transformed to yield $\partial^2(\hat{n} \times \bar{u})/\partial t^2$ and, by use of (44), u_x and u_y at the next time point. The normal component of the $(\nabla \times \bar{u})$ equation yields the normal component of $(\nabla \times \bar{u})$. Five quantities appear under the integral sign: $(\nabla \cdot \bar{u}_3)$, $\bar{u}$, and $(\nabla \times \bar{u})_n$.

The equation, which has a lengthy derivation, is written here without proof:

$$(1 + \varepsilon)(\nabla \times \bar{u})_n \hat{n} - \frac{\gamma}{2} \frac{\partial^2}{c_2^2 \partial t^2}(\hat{n} \times \bar{u}) = \tilde{I}_{s2} + I_{NS} \qquad \text{(A-11)}$$

where

$$\tilde{I}_{s2} = -\left(1 + \frac{\varepsilon}{2}\right)(\nabla \times \bar{u})_s - \frac{\gamma}{2} \frac{\rho_3 c_3^2}{\rho_1 c_2^2} \hat{n} \times \nabla(\nabla \cdot \bar{u}_3) + \frac{\hat{n} \times \bar{u}}{\gamma} - \frac{3}{8} \gamma \nabla_s^2(\hat{n} \times \bar{u})$$

$$- \frac{1}{4} \gamma \hat{n} \times \nabla(\nabla_s \cdot \bar{u}) - \gamma\left(\frac{K_1 - K_2}{4}\right)\left(\hat{n}\left(\frac{\partial u_x}{\partial y} + \frac{\partial u_y}{\partial x}\right) + \hat{x} \frac{\partial u_n}{\partial y} + \hat{y} \frac{\partial u_n}{\partial x}\right),$$

$$I_{NS} = \frac{1}{2\pi} \int_{NS} \left\{ \left(\frac{2L_2}{R} + \frac{1}{Rc_2^2} \frac{\partial}{\partial t^2} \right) (\hat{n} \times \bar{u}') - \hat{R} L_2 (\nabla \times \bar{u}')_n \right.$$

$$\left. + (\hat{n}' \times \hat{R}) \left[\frac{\rho_3 c_3^2}{\rho_1 c_2^2} L_2 (\nabla \cdot \bar{u}_3') - 2 O_2 (\bar{u}' \cdot \hat{R}) \right] \right\} dS' .$$

The solution procedure can thus be summarized:

at time t,

(1) Evaluate the non-self integrals for the three equations (2 scalar and one vector equation), using the retarded values of the five stored quantities $(\nabla \cdot \bar{u}_3)$, $\bar{u}$, $(\nabla \times \bar{u})_n$.

(2) Evaluate the self-terms involving surface derivatives of $\bar{u}(t)$, where $\bar{u}(t)$ had been established at the previous time iteration.

(3) Solve (A-9) and (A-1) for $\nabla \cdot \bar{u}_3(t)$ and $u_n(t + \Delta t)$

(4) Use $\nabla \cdot \bar{u}_3(t)$ to evaluate the remaining term in $\tilde{I}_{s2}$ of (A-11)

(5) Solve (A-11) for $(\nabla \times \bar{u})_n$ (t) and $u_x(t + \Delta t)$, $u_y(t + \Delta t)$.

The process is now repeated for the next time point.

The quantity $(\nabla \times \bar{u})_n$ can also be found by surface differentiation of u_x and u_y, and hence can be eliminated entirely from all the equations. It is thus possible to solve the problem using only four stored quantities. (The only reason $(\nabla \times \bar{u})_n$ is calculated and stored in this formulation is that it is anticipated that this quantity may give rise to difficulties in the solution, since it is overdetermined.) We might expect from physical considerations that four quantities is all that is required: Inside the solid the vector field $\bar{u}$ (which satisfies a wave equation) is specified by 6 quantities on the surface (for instance, $\bar{u}$ and its normal derivative); outside, in the fluid medium, the scalar field $(\nabla \cdot \bar{u}_3)$ or P^e is specified

by 2 quantities on the surface. Now, the boundary conditions impose 4 relations among these quantities, leaving a net of 4 independent quantities. It is seen above that the equations involving only 4 quantities are considerably more complicated than the more natural formulation involving 10 quantities.